2021

Statistics Of Particle Diffusion Subject To Oscillatory Flow In A Porous Bed

Kelly Curran
University of Vermont

STATISTICS OF PARTICLE DIFFUSION SUBJECT TO OSCILLATORY FLOW IN A POROUS BED

A Thesis Presented

by

Kelly Curran

to

The Faculty of the Graduate College

of

The University of Vermont

In Partial Fulfillment of the Requirements
for the Degree of Master of Science
Specializing in Mechanical Engineering

August, 2021

Defense Date: July 16, 2021
Thesis Examination Committee:

Jeffrey S. Marshall, Ph.D., Advisor
George F. Pinder, PhD., Chairperson
William F. Louisos, Ph.D.
Cynthia J. Forehand, Ph.D., Dean of the Graduate College

ABSTRACT

Enhanced diffusion of a suspended particle in a porous medium has been observed when an oscillatory forcing has been imposed. The mechanism of enhancement, termed *oscillatory diffusion*, occurs when oscillating particles occasionally become temporarily trapped in the pore spaces of the porous medium, and are then later released back into the oscillatory flow. This thesis investigates the oscillatory diffusion process experimentally, stochastically, and analytically. An experimental apparatus, consisting of a packed bed of spheres subjected to an oscillatory flow field, was used to study the dynamics of a single particle. A variety of statistical measures were used and developed to characterize the diffusive process. A stochastic model was developed and showed great agreement with the experimental results. The experimentally validated stochastic model was then compared to an analytic prediction for diffusion coefficient from the continuous-time random walk (CTRW) theory for a range of physical and numerical parameter values. Good agreement between the stochastic model and CTRW theory was observed for certain ranges of parameter values, while differences of predictions are discussed and explained in terms of the assumptions used in each model. Results of the paper are relevant to applications such as nanoparticle penetration into biofilms, drug capsule penetration into human tissue, and microplastic transport within saturated soil.

TABLE OF CONTENTS

LIST OF TABLES

LIST OF FIGURES

CHAPTER 1: MOTIVATION AND OBJECTIVE

1.1. Motivation

The problem of diffusion of particles immersed in a porous medium is applicable to many fields. Furthermore, it has been experimentally observed in a number of contexts that imposing an oscillatory flow field (e.g., via an acoustic signal) on particles in a porous medium has increased their effective diffusion coefficient, allowing the particles to penetrate farther and faster than previously able (Ma et al., 2015; Paul et al., 2014). The mechanism facilitating this enhanced diffusion has been identified as a form of bulk diffusion termed *oscillatory diffusion* (Balakrishnan and Venkataraman, 1981b; Marshall, 2016).

Oscillatory diffusion occurs when a particle, in an oscillatory flow field, experiences random hindering, due to interactions with the surrounding porous medium, that either reduces the particle's velocity below that of the surrounding flow field or completely stops the particle. This process, averaged over an ensemble of particles, resembles a diffusion process (Marshall, 2016). A visual representation of this process is shown in Fig 1.1, where two particle paths are shown with one particle freely oscillating (blue) while the other particle experiences hindering due to a porous medium (red). Both particles are subjected to the same oscillatory flow field (v_f). The figure shows the particle position as a time series, with arrows indicating the direction of the flow field. At the initial time (t_0), both particles start at the same y-position (y_0), with velocity oriented in the positive y-direction. Both particles oscillate in phase together until the red particle becomes stuck in one of the pores at time t_1. This hindering of the red particle causes the blue particle to travel farther than the red particle during this time, resulting in an offset. Once the flow

field changes directions, the red particle is released and can now move with the flow field in phase with the blue particle, but the offset in the y-direction remains. The corresponding particle trajectories are also plotted in Figure 1, with the red line corresponding to the hindered (red) particle and the blue dashed line corresponding to the freely oscillating (blue) particle. It is observed that the process of the red particle being stuck for a period of time and then re-entering the flow allows for it to travel further from the initial y-position (y_0) than is the case for the blue particle, which simply oscillates up and down with the flow field. As the process is repeated with increasing time, the hindered (red) particle can drift further and further away from its initial position. Applying this process to a finite number of particles leads to a bulk diffusion away from the initial particle location y_0. While the oscillatory diffusion phenomenon is qualitatively understood, an improved quantitative understanding of the phenomenon would aid in development of methods that utilize an oscillating flow field to enhance diffusion in porous media.

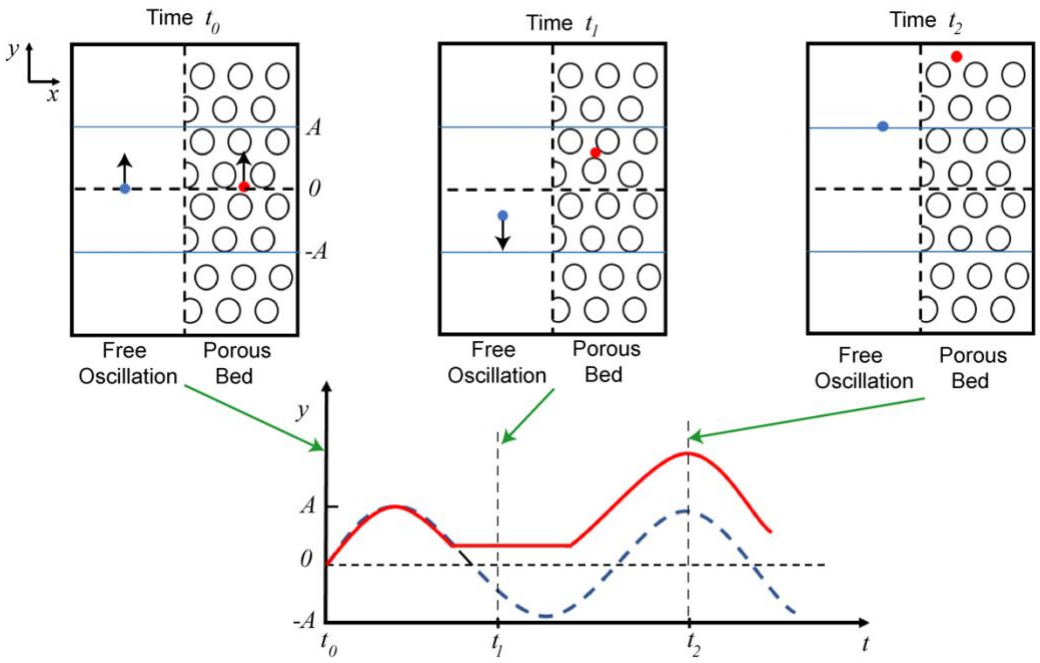

Figure 1: Schematic diagram comparing a freely oscillating particle (blue) and oscillatory diffusion of a particle in a porous bed (red), both subject to the same oscillating fluid velocity field $v_f(t)$.

1.1.1 Biofilms

A common porous medium of significant interest to several important applications is a biofilm. Biofilms are diverse colonies of microbes that are given structure by a polymeric matrix (EPS). The EPS, shown in Figure 2, is primary composed of polysaccharides, which allow bacteria to bind to various surfaces and survive environments that would be lethal for bacteria in a free-floating (planktonic) state. The EPS matrix also provides resistance to common eradication techniques such as antimicrobial agents or host organism immune defenses, which make treating diseases such as cystic fibrosis or tuberculosis more intensive (Hunter et al., 2008). Biofilms are also commonly found on medical equipment such as catheters, prosthetic heart values, and intrauterine devices, increasing the risk of infection. In the food industry, biofilms can be found on processing

equipment, increasing the likelihood of contamination (Kokare et al., 2009). The resistance to various antimicrobial agents that the EPS provides poses a major threat to the pharmaceutical industry as well as industries affected by the presence of biofilms, thus finding methods to mitigate biofilms is of great interest.

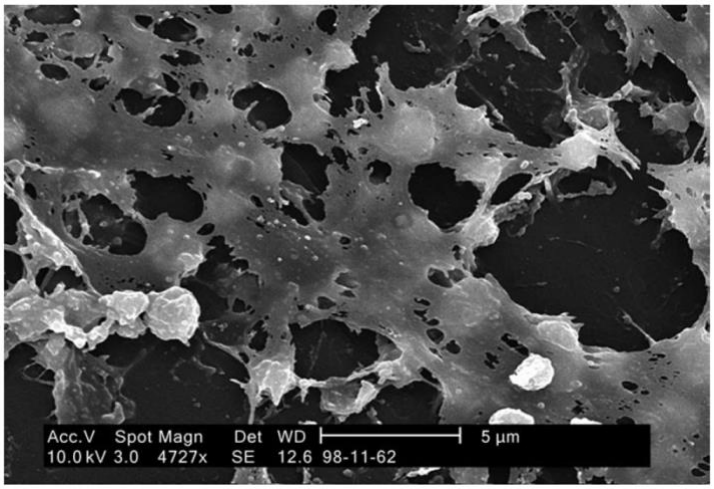

Figure 2: Magnified electron micrograph of a biofilm of Staphylococcus aureus bacteria found on the luminal surface of an indwelling catheter (Hunter et al., 2008).

Ultrasound has been used to mitigate biofilms in a process that has been called ultrasound histotripsy. This process attempts to use high intensity focused ultrasound to break down the EPS. This is done by inducing acoustic cavitation in the water present in biofilm which produces enough energy to cause cell damage, a diagram illustrating this process is provided in Figure 3 (Bsoul et al., 2010). Acoustic cavitation is the process of microscopic gas bubbles forming due to the local pressure drop, from an ultrasonic wave, to below the vapor pressure of the liquid. Once the bubbles form, they collapse producing a large concentration of energy. Using this method to treat biofilms has been studied and is found to increase biofilm removal and in some cases completely eradicate them (Bigelow et al., 2009; Bsoul et al., 2010). Though this method is very promising for removing

biofilms from non-organic surfaces, it requires a large amount of energy and there is clinical concern due to the tissue damage observed in testing.

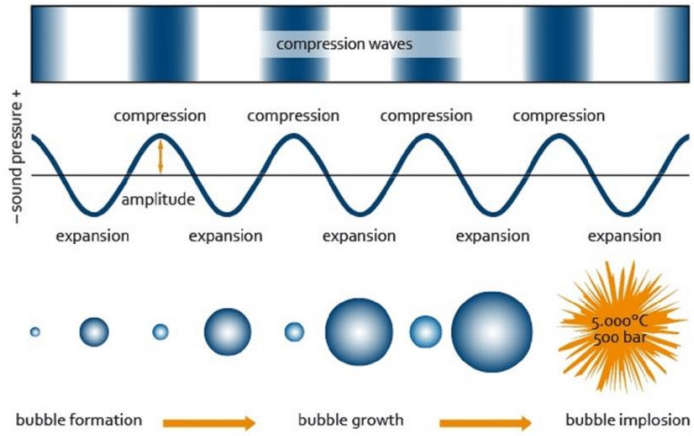

Figure 3: Schematic diagram of cavitation bubbles formation, growth, and implosion due to an ultrasonic wave (Johansson et al., 2017).

A low energy biofilm mitigation approach was developed by using low intensity ultrasound ($< 3\,W/cm^2$) with an antimicrobial agent to eradicate biofilms. It was found that the oscillatory flow field imposed by the ultrasound coupled with the antimicrobials can enhance the degradation of biofilms (Pitt et al., 1994; Qian et al., 1996; Qian et al. 1997; Rediske et al., 1999). Due to the lower power density used, the degradation of the biofilm is not due to the intensity of the ultrasound, but instead is hypothesized to be due to the enhanced transport of the microbial agents (Qian et al., 1996; Qian et al., 1997). This method has been proven *in vivo* by significantly reducing populations of *Escherichia coli* in rabbits, which is usually found on prosthetics (Rediske et al., 1999). Given the porous nature of biofilms, the process enhancing the diffusion of these antimicrobials is thought to be an oscillatory diffusion process where the antimicrobials are transported into the biofilm due to intermediate hindering caused by the EPS.

Antimicrobial administration can be further improved by encapsulating the antimicrobial agents in a nanoparticle. Nanoparticles, examples show in Figure 4, are submicron (< 100nm) spherical particles, typically liposomes or polymer hybrids, which provide shielding to reduce the interaction between the drugs and media, until such time that the contained medium is released. This shielding allows the antibiotic to penetrate farther than un-encapsulated antimicrobial agents, which decreases the amount of agent needed and allows a higher concentration of drugs to be administered at infected sites without losing some of the bulk antibiotic during transport. The nanoparticles have also been shown to circumvent some of the resistance mechanisms that biofilms use to reduce the diffusion of antimicrobial agents (Cheow et al., 2011; Forier et al., 2014). The enhanced efficacy of this method has been shown to improve the thrombolytic effect, used to break down blood clots, when compared to an un-encapsulated agent with the same ultrasonic treatment (Tiukinhoy-Laing et al., 2007).

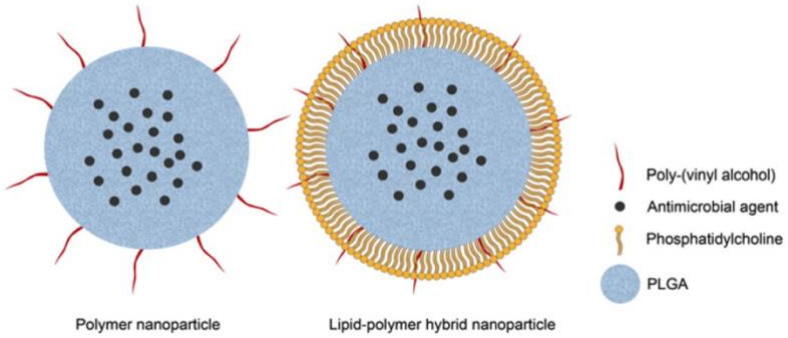

Figure 4: Schematic representation of polymer and lipid–polymer hybrid nanoparticles (Forier et al., 2014).

1.1.2 Targeted Drug Delivery

Another application of interest that utilizes an oscillating flow field to enhance particle transport is targeted drug delivery methods. Traditional drug delivery methods introduce the medicine to the vascular system, orally or intravenously, where it will be carried through the body and eventually reach the disease site (Figure 5). Unfortunately, this method requires more drug than needed to treat the diseased cells and exposes healthy tissue to the drug (Bertrand et al., 2011).

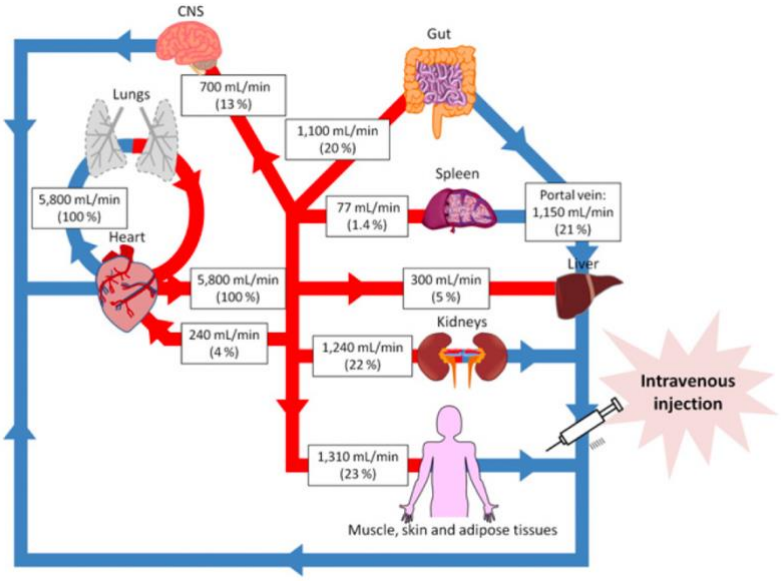

Figure 5 Schematic of drug flow path through the human body after intravenous injection. (Bertrand et al., 2011).

Targeted drug delivery aims to deliver a higher concentration of drug directly to disease sites and minimalize exposure of healthy tissue to the drug. This is accomplished by using nanoparticles as drug delivery vehicles, which can travel to diseased sites before releasing their payload. The most common nanoparticles used for this method are liposomes because they are biocompatible, biodegradable, and are undetectable by the host.

Targeting can be done either passively or actively. Passive targeting utilizes the enhanced permeability and retention (EPR) effect, which suggests that nanoparticles are more likely to accumulate in diseased cells, while active targeting needs information about the diseased cells so that compatible receptors can be added to the nanoparticle to promote bonding (Bae et al., 2001; Singh et al., 2009). Drug release can then be initiated by decomposing the nanoparticle membrane, typically educed by the local environment of the diseased tissue. Drug release can also be initiated by rupturing the nanoparticle, which is typically done with high-intensity ultrasound (Figure 6). (Schroeder et al., 2009; Paul et al., 2013).

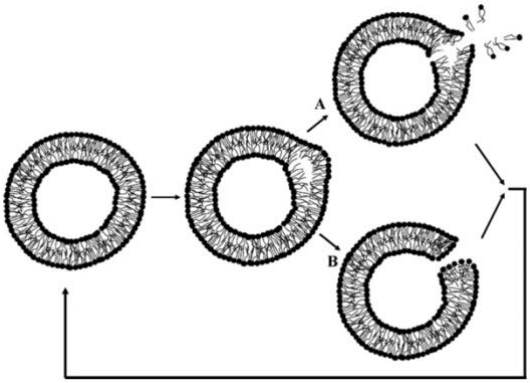

Figure 6 Schematic of nanoparticle (liposome) membrane rupturing by ultrasound with (A) corresponding to a hydrophobic membrane while (B) corresponds to a hydrophilic membrane (Schroeder et al., 2009).

Efforts have been made to diffuse the nanoparticles into the diseased tissue before drug release to administer a more homogeneous drug distribution, rather than simply allowing the nanoparticles to collect on the surface of the diseased tissue. Pitt et al. (2004) demonstrated experimentally that low intensity ultrasound (lower than needed to rupture the nanoparticle) can enhance transport of nanoparticles in tissue. This effect has been found to improve the thrombolytic effect, used to break down blood clots, when compared

to an un-encapsulated agent with the same ultrasonic treatment (Tiukinhoy-Laing et al., 2007).

1.1.3 Other Applications

There are a variety of other applications involving particle transport in porous media of various types, for which particle diffusion plays an important role. While oscillatory diffusion has not been employed in these applications to date, the potential exists that application of an oscillatory flow field (such as an acoustic field) could also be beneficial in enhancing particle diffusion in such applications. One such application of particular interest is the removal of microplastic particles from soil. Microplastics (MPs) are very small plastic particles ($< 5\text{mm}$) that are generated by processes such as plastics manufacturing, sewage treatment, and agricultural systems (Corradini et al., 2019; Fu et al., 2020). These MP's typically end up in marine environments, but they have more recently been identified as a major environmental issue in terrestrial soil (Huffer et al., 2019). The issue with MPs in soil is that their size allows them to be consumed by soil dwelling organisms, which can have a negative impact on agricultural production and has the potential to introduce plastic into the food chain (Rillig et al., 2012, Rillig et al., 2017). The presence of MPs have also been found to effect organisms that play an important role in modifying the soil system (Kim et al., 2019, Souza Machado et al., 2019). A large effort is put on accurately and effectively extracting microplastics from samples for study (Wang et al., 2018; Fu et al., 2020). Development of techniques for effective removal of microplastics from soil is an on-going challenge, but oscillatory diffusion might prove to be a useful method to enhance transport of microplastics out of a layer of soil.

1.2 Objective and Scope

The objective of this thesis is to provide a fundamental quantitative understanding of oscillatory diffusion by studying the individual dynamics of a particle in a packed bed of spheres subjected to an oscillatory flow field. An experiment in which a series of tests observing individual particle motion subject to oscillatory flow has been conducted, in which the particle diameter and the frequency and amplitude of the oscillatory flow are varied. A statistical analysis of the particle response to the oscillatory flow was conducted, describing both the freely oscillating motion of the particle and the period of particle hindering by the surrounding porous bed. The results from the experiment were used to improve and validate a stochastic model and to validate a previously developed continuous time random walk (CTRW) theory for oscillatory diffusion (Balakrishnan and Venkataraman, 1981b).

A literature review related to hindered diffusion and oscillatory diffusion of particles in porous media is provided in Chapter 2. The experimental apparatus and methods are explained in Chapter 3. The statistical measures used for data analysis are presented in Chapter 4. The experimental results are discussed in Chapter 5. A stochastic model of oscillatory diffusion is introduced in Chapter 6. A parametric study comparing parameter sensitivities for both the stochastic model as well as the CTRW theory is presented and discussed in Chapter 7. Conclusions are provided in Chapter 8.

CHAPTER 2: LITERACTURE REVIEW

2.1 Particle Hindering Mechanisms

Oscillatory diffusion relies heavily on the ability of the surrounding porous media to suppress or hinder the motion of the diffusing particles. It is, therefore, important to understand the various hindering mechanisms that come into play for porous media of different types. Hindered diffusion occurs when a diffusing particle is slowed down as it approaches the surface of the porous medium in which it is embedded. This hindering of the particle motion can occur via a variety of different forces imposed on the diffusing particle by the fluid and/or directly by the surrounding porous medium, including hydrodynamic drag, friction, van der Waals adhesion, electrostatic interactions, etc. The influence of this local forcing causes the particles diffusion rate to be reduced or temporarily stopped. Hindered diffusion is commonly observed in systems involving porous media diffusion of colloidal particles, such as microplastics in soil or passive particle filtration processes.

2.1.1 Mechanical Filtration

The most pertinent hindering mechanism to this study is mechanical filtration. This occurs in porous media when the diffusing particle enters a pore that is smaller than the particle in diameter, as shown in Figure 7, causing the particle to become trapped. Filtration has also been observed to occur in pores that are larger than the individual particle diameter, due to formation of particle clusters, as is also shown in Figure 7. This mode of particle hindering is largely dependent on the pore size distribution of the porous media and the size distribution of the diffusing particles. For this reason, many researchers use the ratio of the particle hydrodynamic radii to the mean pore size to classify the strength of this

mechanism. The pore size is measured either experimentally, e.g., if using a natural media (sand, biofilm, agarose gel, etc.), or geometrically assuming an equilateral triangle between three co-planar spheres, as shown in Figure 8. The latter method provides a minimum pore size when the porous medium is composed of a packed bed of spheres. Due to the dependency on the particle-pore size ratio, hindering by filtration typically only occurs when the mean particle diameter of the suspension is near, or larger than, the mean pore diameter of the media, except for in the case of particle clustering.

Figure 7: Illustration particle hindering by mechanical filtration with the black filled circles representing the particles and the unfilled ovals represent the pores (Kuzmina and Osipov, 2006).

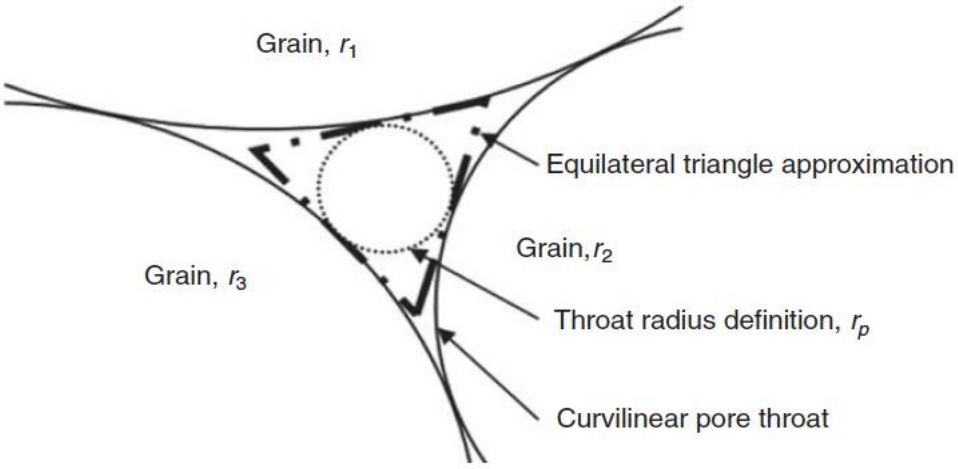

Figure 8: Cross section of pore, showing the equilateral triangle approximation used to estimate the pore diameter (You et al., 2013).

The particle-pore diameter ratio has been shown to help classify different regimes of behavior for particle in porous media. Gerber et al. (2018) examined the transport of spherical polystyrene beads in a packed bed of glass spheres and found that adjusting the particle-pore ratio not only determined when the particles would begin to be trapped in the pores, but also determined the transition to formation of particle caking, a critical issue in water reclamation systems (Wang et al., 2018) where the particles can no longer penetrate the bed and accumulate at the inlet. Mechanical filtration has also been observed to alter the flow conditions of the porous media. As particles become trapped in the pores, the porosity and permeability of the porous medium is reduced. By blocking smaller pores, the flow is redirected toward larger pores, creating preferential pathways. This phenomenon was observed by Sirivithayapakorn and Keller (2003), while studying the transport of fluorescent latex spheres in a silicon micromodel of fine sand, as shown in Figure 9.

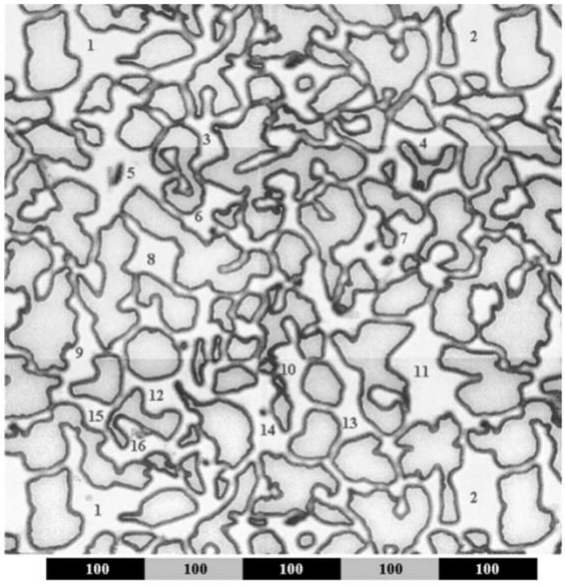

Figure 9: Composite image of the etched repeat pattern in a micromodel of sand, measuring approximately 509 X 509 mm and etched to a depth of about 15 mm. Pore throats are on the order of 3–20 mm in diameter and the pores may be up to 50 mm across. The pattern is repeated 100x100 times in the micromodel, forming a square domain, with the inlet and outlet ports on each of the corners (Sirivithayapakorn and Keller, 2003).

2.1.2 Straining

Another important hindering mechanism is straining, which can be thought of as a combination of mechanical filtration and adhesive capture (Bradford et al., 2002; Bradford et al., 2003; Bradford et al., 2006; Cu et al., 2006; Porubcan et al., 2011). In this process, particles enter the smallest region of a pore space at a surface-surface contact where they become trapped, as shown in Figure 10 (Bradford et al., 2006). This entrapment is due to frictional forces between the particles and surfaces as well as attracting adhesive forces between the particle surface and the surface of the porous medium. This form of hindering has been shown to be important in filtration systems of colloidal particles in porous media. Straining has been suggested to improve agreement between the established theory describing colloidal hindering, known as Clean Bed Filtration Theory (CBFT), and experimental observations. Including straining as a deposition mechanism has been found to reduce error between experimental data and models significantly (Bradford 2003). Like mechanical filtration, the effects of straining are estimated by the ratio of particle to pore size, where straining is most likely to occur in cases where this ratio is very small.

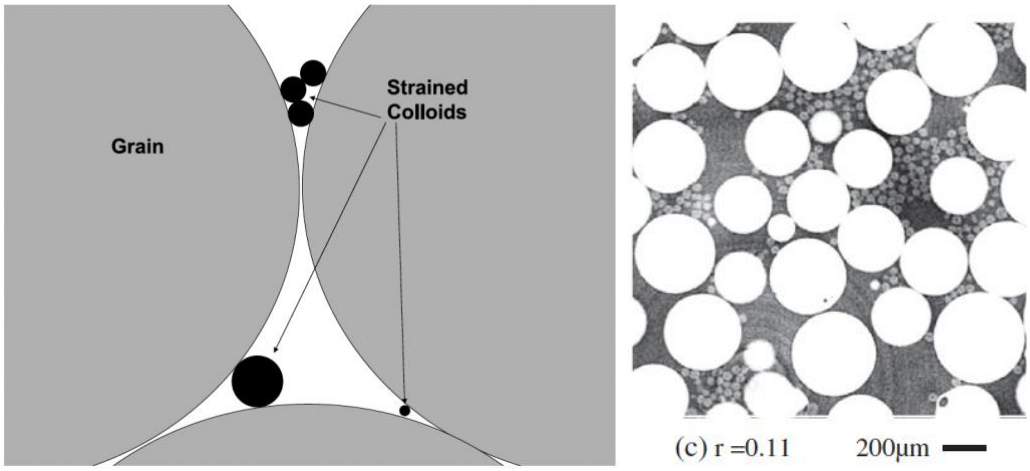

Figure 10: (right) Illustration of strained colloids in the smallest regions of the soil pore space formed adjacent to points of surface-surface contact (Bradford et al., 2006); (left) image of particle straining of spherical polystyrene beads in a packed bed of glass spheres, with the white corresponding to the surfaces (grains) and the light grey corresponding to the beads (Gerber et al., 2018).

2.1.3 Hydrodynamic Hindering

When a particle enters the vicinity of a solid-fluid interface within the porous medium, an increase in hydrodynamic drag is experienced by the particle. This increase in drag is due to both to the fact that fluid velocity near the porous medium boundary has a lower magnitude than within the bulk fluid, as well as to the increased shear stress in the narrow gap between the moving particle and the porous medium boundary. Figure 11 shows a typical velocity profile of fluid flowing in a channel, where the fluid velocity is reduced closer to the channel walls. Hydrodynamic drag is most effective when the flow is laminar, and the viscosity is high. This form of hindering is used in the separation process of microplastics, where microplastics are allowed to flow through a bed of packed spheres, shown in Figure 12. Due to the size range of microplastics (typically $10\text{-}1000\,nm$), the larger particles are less affected by the drag and remain near the center of flow field, while

the smaller particles are more readily hindered by the boundary layer and are brought close to the walls, where adhesion can capture them (David et al., 2019, Fu et al., 2020).

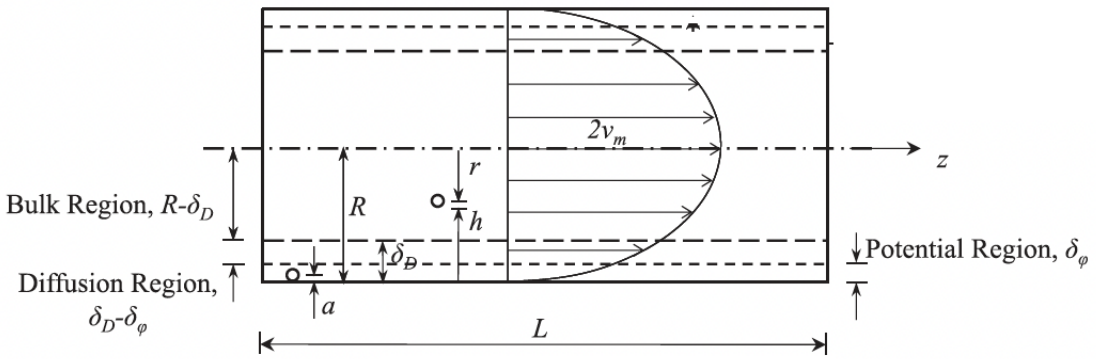

Figure 11: Diagram of velocity profile near surfaces, with the bulk region, diffusion region, and potential region identified (Seetha et al., 2015).

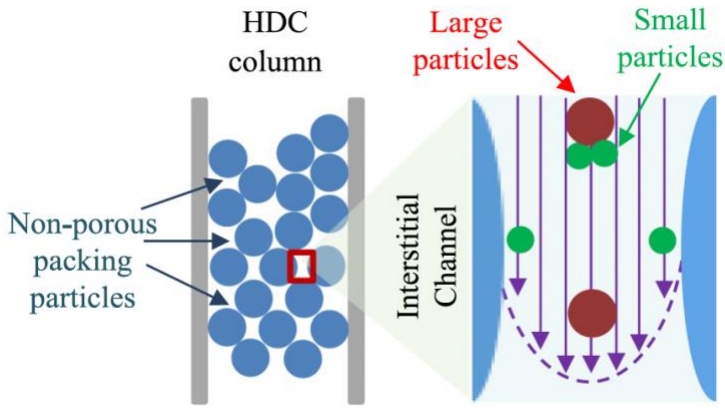

Figure 12: Schematic of microplastic filtration techniques which utilize hydrodynamic drag to hinder particles (Fu et al., 2020).

2.1.4 Adhesive Capture

A major hindering mechanism for low velocity flows with small particles is adhesive capture. Adhesion can occur from van der Waals force (due to dipole interactions) as well as by electrostatic forces between the particle and porous media surfaces. The theory formulated to describe these surface-surface interactions in an ionic liquid is known as Derjaguin–Landau–Verwey–Overbeek (DLVO) theory. The electric double layer (EDL) is formed when ions within the liquid are attracted to the surface of a charged body. These ions tend to form in layers, with the first layer (the surface charge) consisting of ions of the opposite charge as the body which are adsorbed onto the body surface and the second layer (the diffuse layer) consisting of ions of the same charge as the body which are attracted to the ions in the first layer. The effect of these two layers is to electrically screen the body charge. When two charged bodies come sufficiently close to each other (typically on the order of tens of nanometers), the EDLs of the bodies can overlap giving rise to an electrostatic force between the bodies. DLVO theory combines this electrostatic force with the attractive van der Waals force to examine the net force acting between the two bodies.

If the charges of the interacting bodies (e.g., a diffusing particle and a porous medium surface) are the opposite, the electrostatic force from the overlapping EDLs is attractive and the interaction is said to be favorable. In this case, the colloidal particles quickly deposit on the surface of the porous medium. If the charge of the two interacting bodies are the same, the electrostatic force from the overlapping EDLs is repulsive and the interaction is said to be unfavorable (Lee, 1991; Pizzi and Mittal, 2003). Plots of the total interaction energy help to explain how and where particle adhesion to the porous medium can occur. Figure 2.7 shows the total interaction energy for cases where the wall and

particle surface charges are (a) opposite and (b) the same. In this plot, a negative force corresponds to an adhesive force and a positive force to a repulsive force. When the charges between the bodies are opposite (Figure 13a), the force between the bodies is always attractive and increases in magnitude as bodies approach each other. When the charges between the bodies are the same (Figure 13b), the force between the bodies is attractive at both large and small distances but may exhibit a region of repulsive force at an intermediate separation distance. The energy required for the bodies to cross this repulsive force region is known as the energy barrier. Capture of a particle by the porous medium under unfavorable conditions is more difficult than under favorable conditions, but not impossible. Figure 14 plots the total interaction energy (green) for a case with an unfavorable condition, in which both a primary and a secondary minimum can be identified. The deep primary minimum occurs close to the wall, whereas the shallower minimum farther from the wall is known as the secondary minimum. Depending on the ionic strength and the particle energy, capture in the primary minimum is possible, but it has been observed that the majority of capture for colloidal particles actually occurs at the weaker secondary minimum (Shen et al., 2007; Tong et al., 2007; Shen et al., 2010).

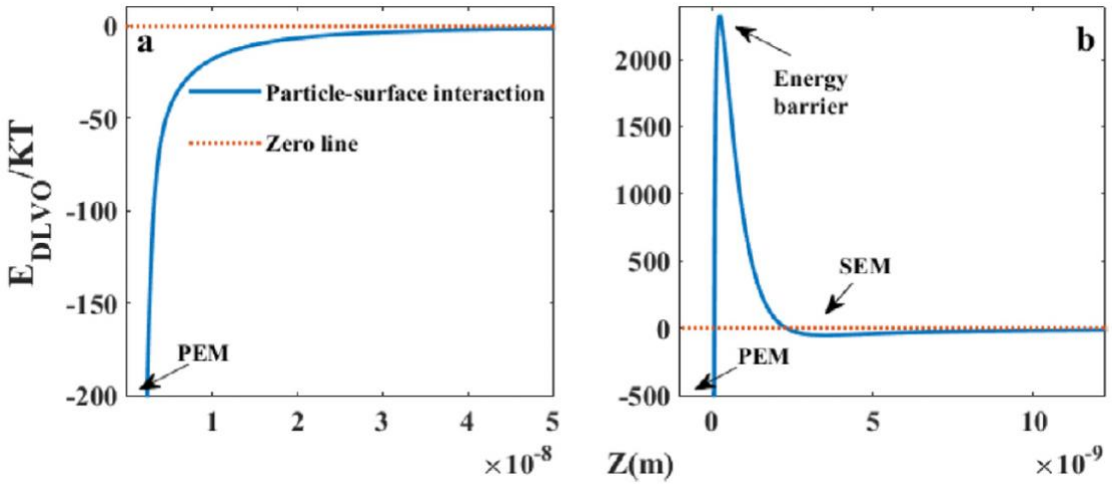

Figure 13: Total particle-surface interaction energy plotted for (a) favorable condition and (b) unfavorable condition. Adhesive forces are negative and repulsive forces are positive (Kermani et al., 2020).

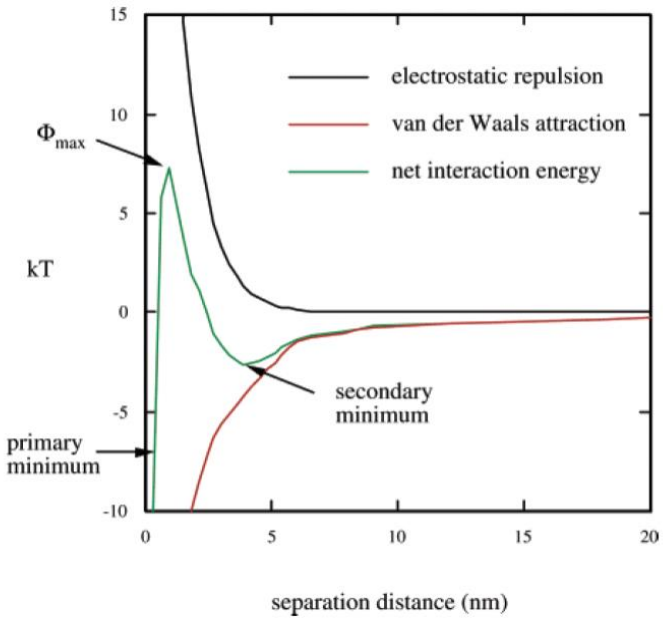

Figure 14: Typical repulsive, attractive, and net interaction energy curves between a sphere and a flat plate based on DLVO theory for an unfavorable interaction (Hahn et al., 2004).

2.2 Hindered Diffusion in Biofilms

The previous section discussed several hindering mechanisms that are present in a large variety of physical systems and processes. To give some prospective on how these mechanisms operate in a specific real-world system, hindered particle diffusion in biofilms is examined in the current section. A biofilm is considered a porous medium due to the surrounding hydrogel formed of the extracellular polymeric substance (EPS) (Miller et al., 2013; Laspidou et al., 2014). Due to the high density of the EPS, flow is restricted through the pores, which are typically on the order of $< 100nm$ (Stewart et al., 2003). This restrictive flow environment means that transport is dominated by diffusion. Biofilms typically have a large water content, in some cases up to 90%, so the diffusion of water (D_w) is typically the reference point when comparing biofilm diffusion. The ratio of the diffusion coefficient within the biofilm (D_b) over that in water is called the relative diffusion coefficient (D_b/D_w). The presence of the polymer matrix in the biofilm has been observed to reduce the diffusion coefficient resulting in a relative diffusion coefficient that is less than unity (Beuling et al., 1998). Several mechanisms have been investigated to understand the hindering effects of a biofilm, most notably mechanical filtration and adhesion. Reaction-diffusion will not be discussed in this review, but it can also be a significant factor for determining penetration depth for reactive substances (Stewart et al., 2003).

2.2.1 Mechanical Filtration in Biofilms

Mechanical filtration is an important hindering mechanism for biofilms. As is typical for a system experiencing mechanical filtration, the particle-pore size ratio plays an important role. The value of this ratio has been studied for several different biofilms and

hydrogel models. Fatin-Rouge et al. (2004) found the critical particle-pore ratio of an agarose gel to be near 0.4, where for values below this ratio anomalous diffusion was observed and for values above this ratio mechanical filtration was observed. Anomalous diffusion refers to diffusion in which the variance does not increase linearly in time, and is typical of Brownian motion in inhomogeneous porous media (Oliveira et al., 2019). Figure 15 shows the two regions of anomalous diffusion, either superdiffusive or subdiffusive, where the particle diffusion rate is either increasing exponentially with time ($\alpha > 1$) or decaying exponentially with time ($\alpha < 1$) respectively. The variance is typically fit with an exponential as shown in (1),

$$\mathbf{log}_{\boldsymbol{n}\to\infty}\langle \boldsymbol{r^2(t)}\rangle \sim \boldsymbol{t^{\alpha}} \tag{1}$$

The exponent (α) is used to classify whether or not a diffusive process is anomalous.

The prediction of anomalous diffusion in biofilms and hydrogels was confirmed by Peulen et al. (2011), who found the diffusion coefficient value for *P. fluorescens* to decrease exponentially with distance into the biofilm, though the anomalous coefficients that were extracted are close to unity, $.89 < \alpha < 1.01$. The prediction of mechanical filtration for particle-pore ratios less than 0.4 was further probed using a range of particle sizes, $40\text{-}550\ nm$ (Forier et al., 2014a). It was found that the particle size cutoff was around $100\text{-}130\ nm$ for *B. multivorans* and *P. aeruginosa*, with particles above this threshold showing almost no penetration into the biofilm.

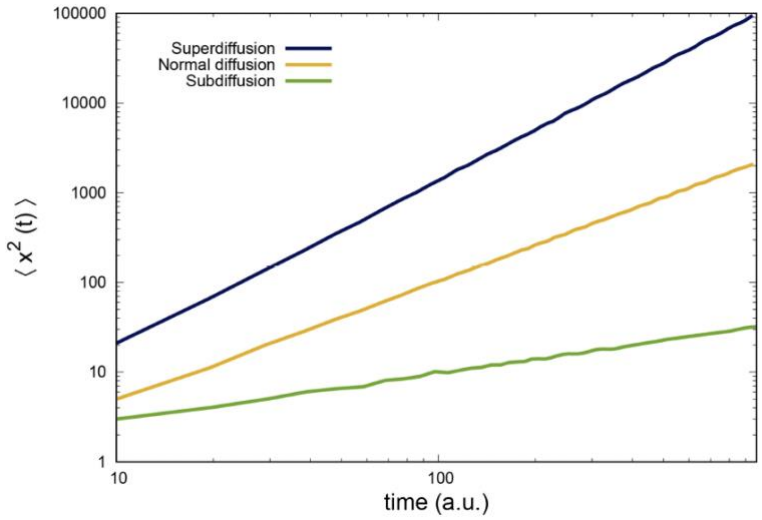

Figure 15: The variance for 3 diffusive processes; superdiffusion α = 1.5 (upper blue curve), normal diffusion α = 1 (middle yellow curve), and subdiffusion α = 0.5 (lower green curve) (Oliveira et al., 2019).

2.2.2 Adhesive Effects in Biofilms

Another significant hindering mechanism of biofilms is the effect of adhesive forces imposed on the particles due to the presence of the EPS. The EPS of most biofilms have a net negative charge, so it would be expected that a negatively charged particle might be given a repulsive cushion while a positively charged particle would be attracted to the walls of the EPS, where they would be deposited. It was found that in fact positively charged particles have an increased diffusion coefficient compared to negatively charged particles in *E. coli* and *S. mutans* (Zhang et al., 2011; Li et al., 2015). It was suggested that the electrostatic repulsion could have effectively reduced the pore sizes experienced by the negatively charged particles, increasing mechanical filtration, while the enhanced diffusion coefficient of the positively charged particles was probably attributed to hydrophobic interactions.

2.3 Oscillatory Diffusion

2.3.1 Analytical Approximations

One of the earliest studies of diffusion in an oscillatory potential was developed to describe the dynamics of ions in superionic conductors. The process was made up of two possible states, (1) short range Brownian diffusion and (2) free oscillation state. The Brownian diffusion is described by the corresponding Langevin equation, given by

$$\boldsymbol{m\ddot{x} + m\gamma\dot{x} - K(x) = f(t)} \tag{2}$$

Here, m corresponds to the particle mass, x is the particles position, γ is the friction coefficient, $\mathrm{K(x)} = -\frac{\partial \mathrm{V(x)}}{\partial \mathrm{x}}$ is the oscillatory forcing, where $V(x)$ is the potential field, and f(t) is the stochastic force. Due to the random nature of Brownian particles, $f(t)$ is modeled as Gaussian white noise with an autocorrelation function given by

$$\boldsymbol{\langle f(t)f(0)\rangle = 2m\gamma k_b T\delta(t)} \tag{3}$$

where k_b is the Boltzmann Constant, T is the temperature, and δ(t) is delta function. The two states are achieved by looking at the temperature extremes. If $k_b T \ll V_0$, then oscillation is dominant, and if $k_b T \gg V_0$, Brownian diffusion is dominant. In-between these limits, both Brownian diffusion and oscillation play a role (Dieterich and Peschel, 1977).

Another approach to describe the dynamics of oscillatory diffusion uses the Fokker-Planck equation. This equation estimates the time evolution of the probability density

functions for stochastic differential equations. Unfortunately, it very difficult to find closed-form analytical solutions to the general Fokker-Planck equation, though several generalized versions have been developed such as the Smoluchowski equation, developed for Brownian diffusion. Solutions to this equation have been found, such as the Hill solution, but due to its assumption of a weak potential there is a limited range of angular velocities and time that can be predicted accurately (Das, 1979).

Continuous time random walk (CTRW) is a generalized random walk theory which treats the time in-between successive steps as a random variable. This theory has been shown to successfully describe many different processes including anomalous diffusion, photon imaging, and financial distributions (Sokolov and Klafter, 2007; Chernomordik et al., 2010; Masoliver et al., 2006). CTRW has also been applied to oscillatory diffusion by Balakrishnan and Venkataraman (1981). They use a two-state model, where the particle is either in a ‘flight’ state when the particle is freely moving between sites or an oscillatory state, when the particle experiences local oscillations at a single site. The time duration that the particle occupies at each state is treated as a random variable, which is called the 'holding time'. Unlike the Langevin or Fokker-Planck methods, the CTRW theory is not restricted to a single dimension and provides closed-form solutions for the diffusion coefficient as well as a number of other parameters.

2.3.1 Experimental Observations

An experimental study examining the effect of an acoustic field on diffusion in a packed bed of spherical beads was reported by Vogler and Chrysikopoulos (2001) for solute diffusion and by Thomas and Chrysikopoulos (2007) for particle diffusion. Thomas and Chrysikopoulos (2007) forced tracer particles through a wet bed of packed spheres

using an ultrasonic transducer. A schematic diagram of the experiment is shown in Figure 16. The concentration of particles was measured at the outlet of the bed as a function of time, allowing for particle speed and peak concentration information to be extracted. It was found that when an oscillating forcing was introduced, the peak concentration measured at the outlet occurred 7% earlier than for the control case but did not alter the concentration distribution significantly. One of the challenges with this experiment is that it does not readily allow the investigator to distinguish between the effect of enhanced diffusion versus that of acoustic radiation pressure (King, 1934).

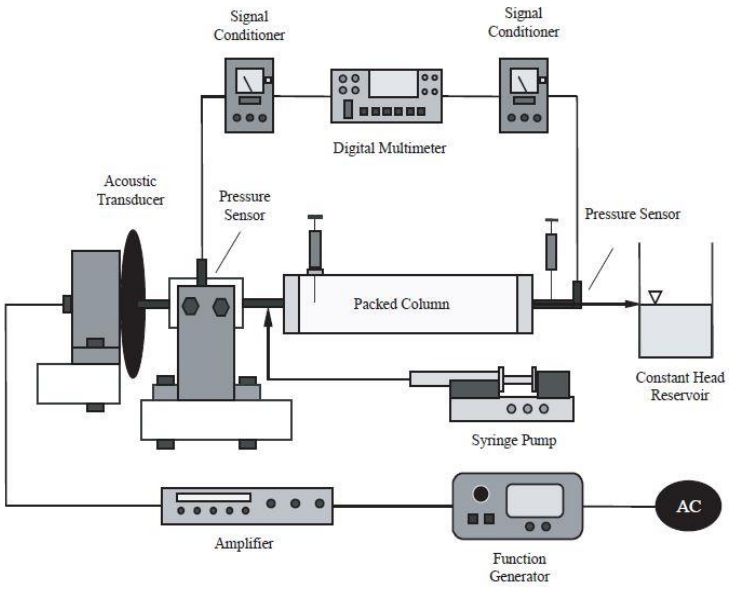

Figure 16: Schematic of experimental apparatus consisting of an acoustic transducer forcing injected tracer particles through a packed bed of spheres (Thomas and Chrysikopoulos, 2007).

Acoustic enhancement of particle diffusion was later observed by Ma et al. (2015) when studying the effect of ultrasound on particle transport to, and penetration into, a hydrogel. A suspension of fluorescent tracer particles was placed above an alginate hydrogel, where the positioning of the ultrasound transducer relative to the hydrogel is

indicated in the schematic diagram in Figure 17. The ultrasound was found to improve transport to the gel surface due to the formation of an acoustic streaming flow. Ultrasound was also observed to increase the penetration of nanoparticles into the hydrogel. Images of a three-dimensional section of the hydrogels showing fluorescence induced by penetrated nanoparticles is shown in Figure 18 for both the control case (with no ultrasound) and for the case with ultrasound treatment. The fluorescent intensity corresponds to the concentration of nanoparticles. The control case appears to have experienced almost no penetration, while the ultrasound-treated case shows significant fluorescence, indicating that a large number of nanoparticles have penetrated into the hydrogel to various depths. The fluorescent intensity was measured as a function of depth, as shown in Figure 19, where an exponential decay can be observed. In a follow up study, Ma et al. (2018) obtained detailed measurements of the effect of ultrasound on the diffusion coefficient for two sizes of nanoparticles (20 and 100nm) diffusing into an agarose hydrogel. The apparatus is similar to the previous study, but now the hydrogel is formed of two layers, one of which is seeded with fluorescent tracer particles and the other of which is unseeded. The experiment measured the rate of diffusion of particles from the seeded layer into the unseeded layer both with no acoustic forcing and in the presence of low-intensity ultrasound forcing. An increase in diffusion coefficient of between 74-133% was experienced with ultrasound compared to the control case (with no ultrasound).

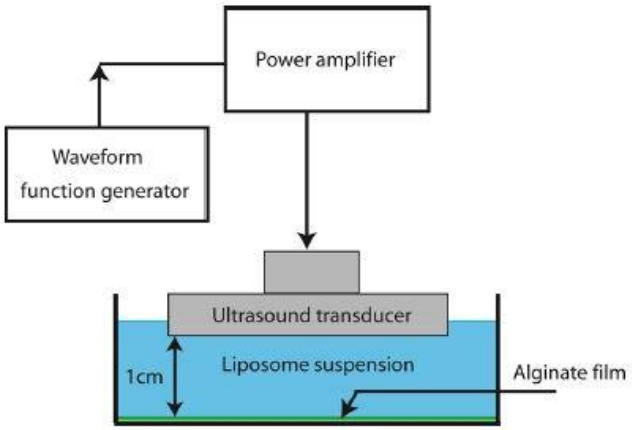

Figure 17: Schematic diagram of the experimental apparatus consisting of an ultrasonic transducer forcing either a liposome or nanoparticle suspension toward an alginate film (Ma et al., 2015).

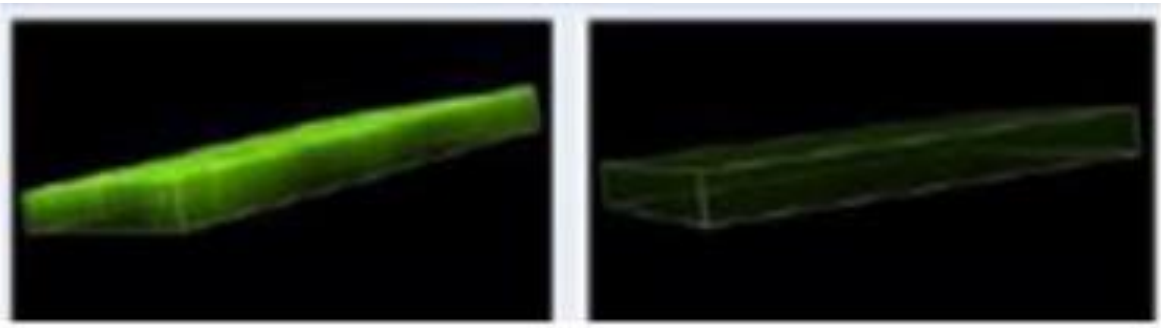

Figure 18: Slices of hydrogels for the ultrasound treated gel (left) and the control gel (right). The fluorescent intensity corresponds to concentrations of tracer particles (Ma et al., 2015).

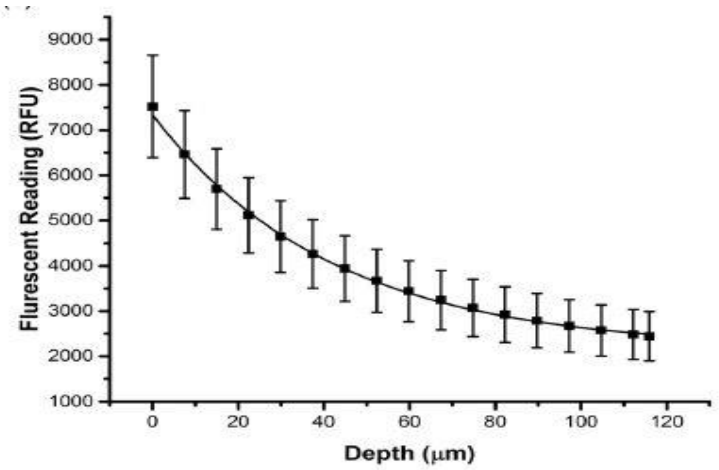

Figure 19: Plot showing the fluorescent intensity with the depth into the hydrogel for the ultrasound treated gel (Ma et al., 2015).

A one-dimensional stochastic model was developed by Marshall (2016) to describe the enhanced diffusion caused by acoustic forcing in the experimental studies mentioned above. The model explains the enhanced diffusion of particles subjected to an oscillatory flow using a combination of a freely oscillating particle state and random hindering state, in which the particle is temporarily captured by the porous medium. In the limit of many time steps, the stochastic model was shown to reduce to a solution of the standard diffusion equation, but where the effective diffusion coefficient was dependent on the acoustic forcing. Figure 20 shows a plot of the predicted probability density function by the stochastic model and the standard one-dimensional diffusion equation. While this model clearly demonstrates the oscillatory diffusion mechanism by which acoustic forcing can act to enhance particle diffusion in a porous medium, it does not connect well with the physics of particle transport through the porous bed. For instance, physical parameters such as particle and pore size do not enter into the model.

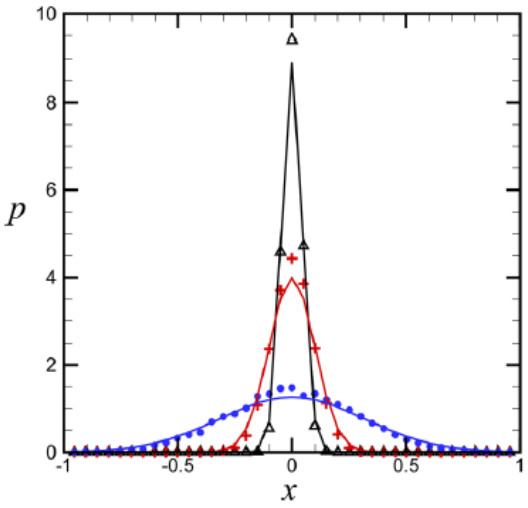

Figure 20: Comparison of predicted probability density functions (PDF) for the stochastic model (symbols) and the one-dimensional diffusion equation (solid line) are plotted. The PDF was capture at three time steps, $t = 2$ (triangles), 10 (crosses), and 100 (circles) (Marshal, 2016).

CHAPTER 3: EXPERIMENTAL METHOD

Experiments examining particle diffusion in a quasi-two-dimensional bed of spheres were conducted using the apparatus shown in Figure 21. The system used a variable-speed motor to oscillate a piston, causing an oscillatory sloshing flow through the porous bed. Details of the motor-piston assembly are shown in Figure 21b. The motor shaft rotation frequency (Iron Horse MTR-P50_3BD18) was controlled using an AC drive (Automation Direct GS1-10P5). The shaft frequency was reduced with a worm gear box (Iron Horse WG-175-005-H) with gear ratio of 5. A 10.2 cm pulley on the motor shaft was connected to a similar pulley on a second shaft (the 'bearing shaft', identified as K in Figure 21b) via a 140 cm V-belt. A crank-and-piston assembly was used to convert the rotational motion of the bearing shaft to vertical motion of the piston. The piston was connected to the rotating bearing shaft via a 19 cm long drive rod (M in Figure 21b), which was connected to the bearing shaft via an amplitude plate (L in Figure 21b). The oscillation amplitude was adjusted by moving the connection point of the drive shaft between five available holes drilled into the amplitude plate, which were located at radial distances of 1.3, 2.5, 4.1, 5.8 and 7.4 cm ($\pm$ 0.1 cm) from the center of rotation of the bearing rod. The drive rod was attached using a ball joint to a vertical 61 cm long threaded piston rod that connected to the piston. The piston was formed from two 1.3 cm PVC end caps and a 1.3 cm coupling, which were sanded to fit inside the 2.5 cm PVC pipe. The threaded piston rod was passed through the piston and was held in place with nuts on each end.

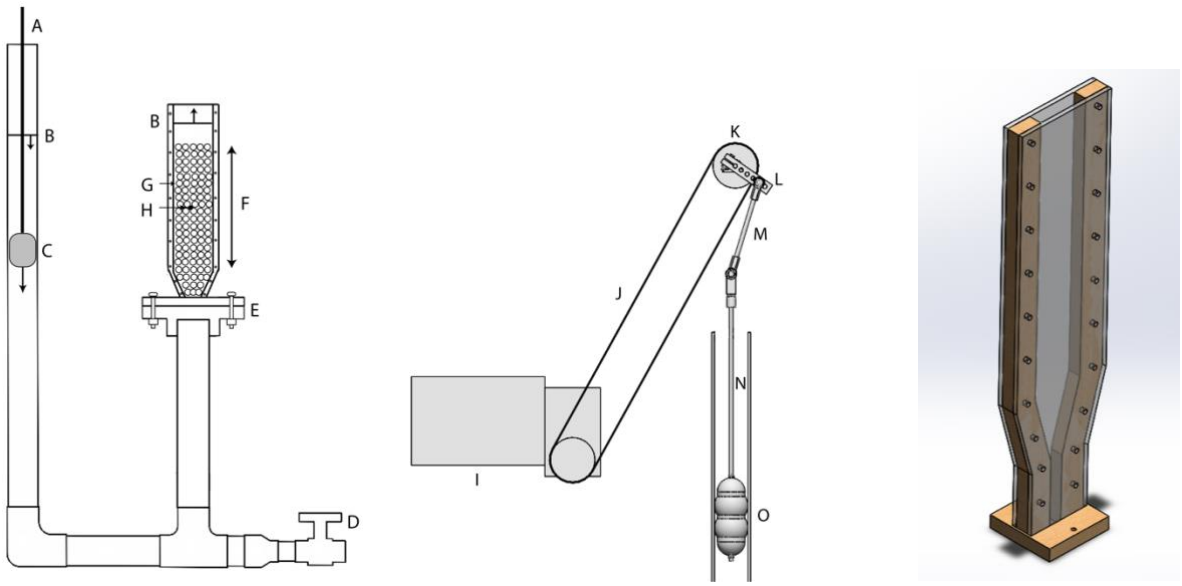

(a) (b) (c)

Figure 21: Schematic diagrams of the experimental apparatus. (a) Overview of apparatus showing [A] piston rod, [B] fluid level, [C] piston, [D] valve, [E] flange, [F] test section, [G] transparent beads, and [H] moving test particle. (b) Close-up of the drive mechanism, showing [I] variable-speed motor, [J] belt, [K] bearings and bearing shaft, [L] bar to set oscillation amplitude, [M] drive shaft, [N] piston shaft, and [O] piston. (c) Close-up of the test section.

Supports were placed below the system and along the sides to hold the system rigidly in place. A PVC ball valve (D in Figure 1a) and exit tube were installed to empty the fluid from the system. The 2.5 cm pipe was connected to a 2.5 cm flange (E in Figure 21a), which was bolted onto the test apparatus. The test apparatus was formed of two polycarbonate sheets with sides formed of oak boards. The test section measured 7.6 cm wide, 1.9 cm thick and 40.6 cm tall, with an additional 10.2 cm long transition section that connects the test section to the flange. The sides of the polycarbonate sheets were coated with 6 mm diameter glass hemispheres. In-between the two layers of hemispheres were placed three layers of borosilicate glass beads with diameter $d_{bead} = 6\ mm$. Pure glycerin was used as the working fluid, which was selected in order to match refractive

index with the borosilicate glass beads, so that the glass beads were transparent in the glycerin. The glycerin had density $\rho_{gly} = 1.26\ g/cm^3$ and viscosity $\mu_{gly} = 0.95\ Pa \cdot s$. The porosity of the packed bed in the test section was measured to be $\phi = 0.334 \pm 0.006$.

The oscillation amplitude y_{amp} is defined as the amplitude that a passive fluid particle would nominally travel within the porous medium in response to the oscillating motion of the piston. Oscillation amplitude was calibrated by first filling the liquid to a height over the top of the porous bed and measuring the amplitude of oscillation y_{fluid} of the fluid interface under the given piston oscillation amplitude and frequency. The nominal oscillation amplitude of a particle within the porous bed is then obtained as

$$y_{amp} = y_{fluid} / \phi . \tag{4}$$

The nominal particle motion within the porous bed (with no particle hindering) is therefore given by the equation

$$y_p(t) = y_{amp} \sin(\omega t) + y_0 , \tag{5}$$

where $\omega = 2\pi f_{osc}$ and f_{osc} is the oscillation frequency. The nominal oscillating velocity can be obtained by taking the time derivative of (5), giving

$$v_p(t) = v_{amp} \cos(\omega t) , \tag{6}$$

where the amplitude of the velocity oscillation is given by $v_{amp} = \omega y_{amp}$. The parameters y_{amp}, v_{amp} and f_{osc} are used for nondimensionalization of the experimental data.

Each experimental run examined motion in the porous bed of a single moving test particle. The test particle was placed approximately mid-depth in the porous bed at the start of each run using a 25.4 cm long hypodermic needle (14 gauge). Each run was repeated nominally 20 times in order to obtain an ensemble of samples. Two sizes of test particles were used in the experiments. The first particle type consisted of fluorescent red polyethylene spheres (Cospheric) with diameter $d_1 = 0.52 \pm 0.03$ mm, sphericity $\Psi_1 = 0.999996$, and density $\rho_1 = 1.22 \pm 0.03$ g/cm^3. The second particle type consisted of black acrylic spheres (Avashop) with diameter $d_2 = 1.3 \pm 0.1$ mm, sphericity $\Psi_2 = 0.996$, and density $\rho_2 = 1.06 \pm 0.02$ g/cm^3. None of the test particles were observed to move a measurable amount when suspended in a bath of stationary glycerin. The particle diameter was measured using an optical microscope (Nikon LABOPHOT-2), from which we obtained both the mean and root-mean-square (rms) values for a sample of 25 particles of each type.

The particle density was obtained by measuring the time required for particles to settle a distance of 6 cm at terminal velocity v_T in a beaker of water, which yielded a terminal velocity of 3.37 ± 0.02 cm/s and 5.10 ± 0.08 cm/s for a sample of 20 particles of type 1 and 2, respectively. The particle density was obtained by an equilibrium condition between drag and gravitational force, giving

$$\rho_p / \rho_w = 1 + \frac{3C_D}{4gd} v_T^2, \tag{7}$$

where for a sphere with Reynolds number $Re_p = \rho_w d v_t / \mu_w$ in the range $Re_p < 800$, the drag coefficient can be approximated using the Schiller-Naumann (1933) correlation as

$$C_D = \frac{24}{\mathrm{Re}_p}(1 + 0.15\,\mathrm{Re}_p^{0.687}) \tag{8}$$

The particle Reynolds number at terminal velocity in water was obtained as 19.96 and 74.49 for particles of type 1 and 2, respectively. The uncertainty in the density measurement was estimated from the measured uncertainties in diameter and terminal velocity, δd and δv_t, using the standard variance equation

$$\delta\rho_p = \left[\left(\frac{\partial \rho_p}{\partial d} \right)^2 (\delta d)^2 + \left(\frac{\partial \rho_p}{\partial v_T} \right)^2 (\delta v_T)^2 \right]^{1/2} \tag{9}$$

The test particles were photographed using a video camera (Sony Handycam) at 30 frames per second, with lighting provided by a 50W LED flood light. The camera was mounted with viewpoint orthogonal to the side of the polycarbonate sheet on the side of the test section. Fiji particle tracking software, with the plug-in TrackMate, was used to track the motion of the moving particles during each experimental run. This software identifies the test particle at each frame of the video sequence and outputs the location in a coordinate frame. Because we experienced some gaps and errors in the automated particle

tracking, we also manually tracked particle paths for each run. The particle location data was used to compute statistical measures of the particle diffusion, as discussed in Chapter 3.

CHAPTER 4: DATA ANALYSIS

The output of the particle tracking software is a string of data indicating the particle position $y(t)$ at times t_i, i = 1,2,3,4,…, in the vertical direction, denoted by y_i. The statistical measures of a diffusion process change as functions of time. The averages in these statistics are taken over repeated realizations of the process (or different experimental 'runs'). We call each of these runs a *string*, and refer to the entire set of strings for a given set of parameter values as an *ensemble*. The ensemble average $f_E(t) \equiv \langle f_n(t) \rangle_E$ and the time average $\bar{f}_n \equiv \langle f_n(t) \rangle_T$ of some quantity $f(t)$ are defined by

$$f_E(t) = \langle f_n(t) \rangle_E \equiv \frac{1}{N_E} \sum_{n=1}^{N_E} f_n(t), \qquad \bar{f}_n = \langle f_n(t) \rangle_T \equiv \frac{1}{T} \int_0^T f_n(t)\, dt, \tag{10}$$

where subscript *n* denotes the string number, N_E is the number of strings forming the ensemble, and (0,*T*) is the time interval over which the data is taken. With this terminology, we define the mean, variance, skew and kurtosis of the particle position as follows:

$$y_E(t) = \langle y(t) \rangle_E, \tag{11}$$

$$y_{\text{var}}(t) = \langle [y(t) - y_E(t)]^2 \rangle_E, \tag{12}$$

$$y_{skew}(t) = \langle [y(t) - y_E(t)]^3 \rangle_E, \tag{13}$$

$$y_{kurt}(t) = \langle [y(t) - y_E(t)]^4 \rangle_E. \tag{14}$$

The mean square deviation (MSD) is based on the difference between the measured signal $y(t)$ and a prescribed predicted signal $y_p(t)$, and it is defined by

$$y_{MSD} = \left\langle \left\langle [y(t) - y_p(t)]^2 \right\rangle_T \right\rangle_E . \tag{15}$$

For a normal random walk process the predicted value might be set to the initial particle height y_0, whereas for oscillatory diffusion the predicted value might be set to an oscillating function of the form (5).

The autocorrelation function $\rho(t)$ provides an indication of the correlation between a signal at the current time and the same function at a previous time, hence giving an indication of the degree to which a signal repeats itself. A height difference function $\Delta y(t)$ is defined by

$$\Delta y(t) = y(t) - y_E(t) , \tag{16}$$

which is equal to the deviation of the particle height from its ensemble mean value. The autocorrelation function is then defined as

$$\rho(\tau) = \left\langle \left\langle \Delta y(t-\tau)\, \Delta y(t) \right\rangle_T \right\rangle_E , \tag{17}$$

where τ is called the lag time.

The power spectrum $e(f)$ describes the spectral make-up of a signal's 'energy' in frequency space. The power spectrum is a plot of the spectral energy density $e(f) = |\hat{y}(f)|^2$ against the frequency f. The power spectrum was computed for each data set, and then averaged over all data sets in the ensemble.

As a baseline, we present examples for these various statistical measures for a random walk process, as is typical of Brownian diffusion. In order to be consistent with the data analysis approach used in our experimental study, we have formed an ensemble with 20 strings and have used a run length with approximately the same number of data points as in the experimental runs. The effective diffusion coefficient for the random walk calculations was $D = 0.000125$ and the time step was $\Delta t = 0.01$, so that the corresponding displacement length ε for each random step was given by

$$\varepsilon = [2D\Delta t]^{1/2} \cong 0.00158 . \tag{18}$$

Several different measures for the random walk computations are plotted in Figure 22, along with theoretical predictions (shown using a dashed line). The ensemble variance $y_{\text{var}}(t)$ is plotted versus time in Figure 22a, and it is found to agree well with the theoretical prediction

$$y_{\text{var}}(t) = 2Dt . \tag{19}$$

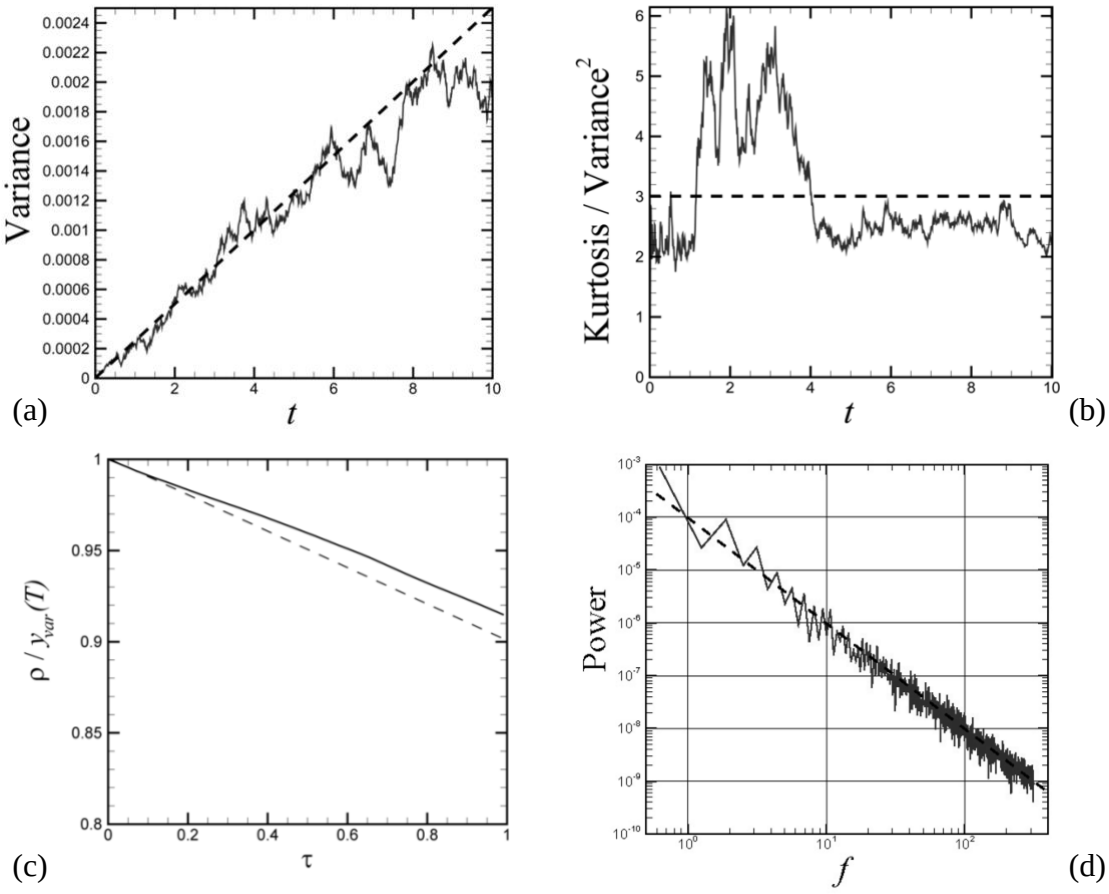

Figure 22: Plots illustrating statistical measures for a random walk process, showing (a) the ensemble variance and (b) the ratio of the kurtosis over the variance squared as functions of time, (c) autocorrelation as a function of time delay, and (d) the power spectrum. Theoretical predictions are plotted as dashed lines.

The mean-square deviation (MSD) for the random walk computation was computed as $y_{MSD} = 0.00127$, which compares well with the theoretical value $y_{MSD} = \langle y_{\text{var}}(t) \rangle_T \cong 0.00125$. The ratio of the kurtosis to the square of the variance is plotted versus time in Figure 22b, and it is compared to the theoretical prediction $y_{kurt}(t) / y_{\text{var}}^2(t) = 3$ for a normally distributed process.

The autocorrelation $\rho(\tau)$ is plotted as a function of the delay time τ in Figure 22c. For a random walk process, if a displacement $y(t)$ has a variance given by (19), then the correlation of $y(t)$ with itself at two times s and t is given by

$$E[y(s)y(t)] = 2D\min(s,t)\,. \tag{20}$$

The theoretical value of the autocorrelation function defined by (17) is a linear function of the lag time τ, given by

$$\frac{\rho(\tau)}{y_{\text{var}}(T)} = \frac{2D(T-\tau)}{2DT} = 1 - \frac{\tau}{T}\,. \tag{21}$$

This theoretical value is shown in Figure 22c to be in reasonably good agreement with the predicted value from the random walk computation. The computed power spectrum (Figure 22d) is consistent with the theoretical prediction $e(f) \propto 1/f^2$ for a random walk process, indicated by the dashed line with slope -2 on the log-log plot.

CHAPTER 5: EXPERIMENTAL RESULTS

The experimental cases listed in Table 1 were analyzed in terms of the statistical measures described in Chapter 4. Results are given below for Case B-2, which is characteristic of the other cases examined. We then focus more on the measures of particle hold-up for the different cases.

Table 1: Parameter values used for the different experimental runs. The uncertainty is ± 1 mm for oscillation amplitude, ± 0.03 mm for diameter of the small particles, and ± 0.1 mm for diameter of the large particles. The uncertainty for frequency is 1% of the recorded value.

Run ID	Test particle diameter d (mm)	Frequency f_{osc} (Hz)	Position amplitude y_{amp} (mm)	Velocity amplitude v_{amp} (mm/s)	Number of repeated runs	Total run time, T/t_{osc}
R-1	0.52	0.15	15.0	14.1	20	260
R-2	0.52	0.25	15.3	24.0	13	138
R-3	0.52	0.50	17.3	54.3	20	1292
R-4	0.52	0.75	12.0	56.5	20	1211
R-5	0.52	0.25	31.0	48.7	21	128
R-6	0.52	0.25	42.9	67.4	20	50
B-1	1.3	0.15	15.0	14.1	21	241
B-2	1.3	0.25	15.3	24.0	20	348
B-3	1.3	0.50	17.3	54.3	20	1846
B-4	1.3	0.75	12.0	56.5	20	3557

5.1 Standard Statistical Measures

After the particle is released in the oscillating flow field within the central part of the porous bed, it is observed to oscillate up and down with the imposed oscillatory flow, but to also intermittently pause in a fixed position for different intervals of time before continuing in oscillatory motion. The particle eventually reaches either the upper or lower boundary of the porous bed, at which time the experiment is stopped. A typical particle

string $y(t)$ is plotted in Figure 23, along with the associated velocity $v(t)$. In order to smooth the data in the presence of experimental noise, we computed velocity using a moving least-square fit to a set of five points surrounding the point at which the velocity is desired (Ghazi and Marshall, 2014). The particle position oscillates with the driving frequency, but with an amplitude that varies with time. There are time intervals where the particle oscillation amplitude is very small, and other times where it approaches the nominal amplitude y_{amp}.

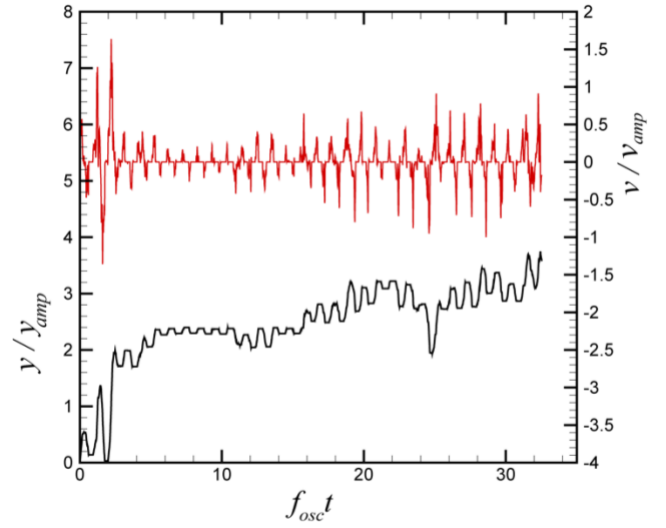

Figure 23: Plot showing time variation of a sample experimental string for $y(t)$ (bottom, left-hand axis) and $v(t)$ (top, right-hand axis) for Case B-2.

The mean, variance, and kurtosis of the particle displacement were computed using ensemble averages over the different particle strings (Figure 24), as discussed in Chapter 4. These ensemble-averaged measures are found to oscillate in time at approximately the driving frequency due to the phase differences between the different particle strings. This effect would be expected to diminish as the number of strings becomes large. The particle mean oscillates in time with a slight upward drift. The variance exhibits a nearly linear increase superimposed on the oscillations, typical of a diffusion process. The ratio of

kurtosis to variance squared ranges between 2 and 3, as was also the case for the random walk process (Figure 22b).

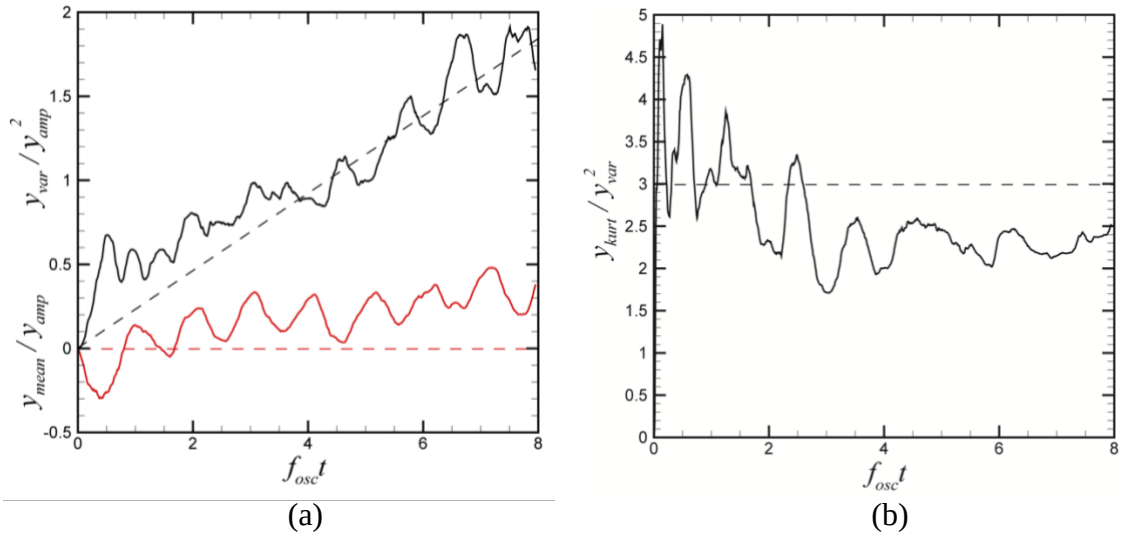

(a) (b)

Figure 24: Plots showing time variation of (a) mean (red) and variance (black) of y position and (b) ratio y_{kurt}/y_{var}^2 for Case B-2. Theoretical results are indicated by dashed lines.

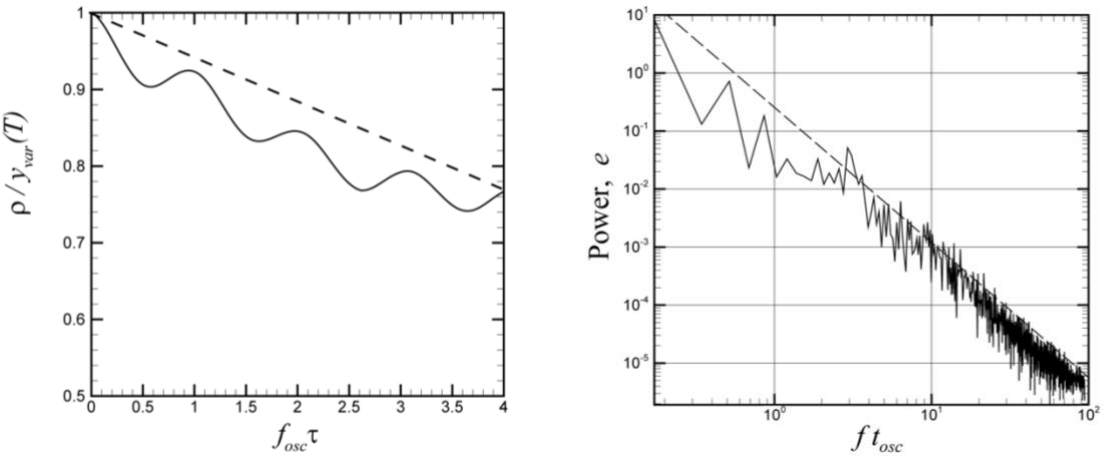

(a) (b)

Figure 25: Plots showing (a) the autocorrelation and (b) the power spectrum for Case B-2. The dashed line in (a) is the theoretical expression in Eq. (15) for a random-walk process, and the dashed line in (b) is for the theoretical power law for random walk diffusion.

The autocorrelation is plotted in Figure 25a as a function of the dimensionless lag time $f_{osc}\tau$. It is noted that for a random walk diffusion process, the autocorrelation is a linear function of lag time with decreasing slope, indicated by the dashed line in Figure 25a. For a purely oscillating process, the signal is perfectly correlated once every oscillation period, and the resulting autocorrelation is an oscillatory function. The curve observed in Figure 25a for an oscillatory diffusion process is a combination of these two trends, consisting of an oscillating function with a downward trending mean value. The power spectrum plotted in Figure 25b is found to be similar to that for random walk processes (Figure 22d), with a variation closely following a line with slope of -2 on the log-log plot, indicating a $e(f) \propto 1/f^2$ power-law dependence with frequency. A probability density function (P.D.F.) for the velocity is plotted in Figure 26 which indicates that the particle velocity varies nearly as a Gaussian function (dashed line), with the exception of a high spike at $f = 0$, indicative of a particle that is not moving (or a 'captured' particle).

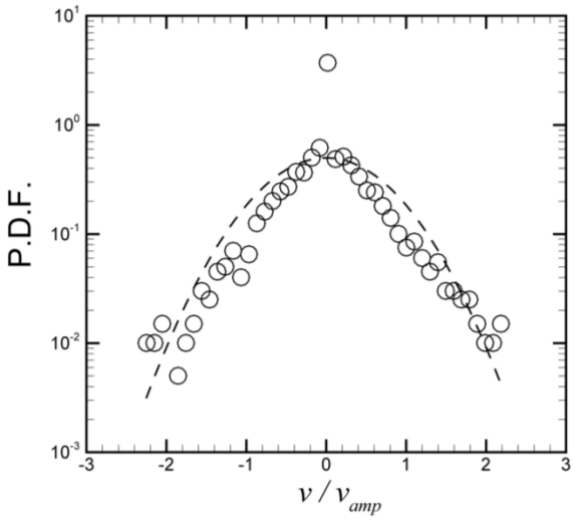

Figure 26: Probability density function of velocity for Case B-2 at time $f_{osc}t = 0.4$. The dashed line is for the Gaussian curve $f(x) = 0.5\ exp(-x^2)$.

5.2 Hold-up Measures

In an oscillatory diffusion process, particles move periodically up and down in the direction of oscillation, while intermittently getting stuck (captured) for random intervals of time. This behavior is in contrast to the simple one-dimensional random walk process, for which the velocity magnitude is equal to a constant value $v = \varepsilon / \Delta t = [2D / \Delta t]^{1/2}$. Particle hold-up is identified by time steps where the absolute value of the particle velocity v is less than a prescribed fraction C_{cut} of the velocity amplitude, or

$$|v| < C_{cut} v_{amp} . \tag{22}$$

When (22) is satisfied we say that the particle is in a captured state, and when it is not we say that the particle is in a free state. For each hold-up event, the hold-up duration time

t_{hold} is set equal to the number of consecutive cycles during which the particle is in a captured state times the time step Δt. The set of hold-up duration times for all strings in an ensemble was sorted into a set of bins, and the number of hold-up events falling in each bin is denoted as $N_{hold,i}$, where the bin number i corresponds to a certain interval of the hold-up duration time t_{hold}. A plot showing the values of the normalized number of hold-up events $N_{hold}/(N_{tot} f_{osc} \Delta t_{bin})$ for these bins is given in Figure 27 for the case B-2, comparing results for C_{cut} values of 0.1, 0.2 and 0.3 for a plot with 50 bins of uniform width. In this plot, N_{tot} is the total number of hold-up events and Δt_{bin} is the bin width. For larger C_{cut} values there are more long-duration hold-up events (with larger values of t_{hold}), whereas for smaller C_{cut} values the long duration hold-up events tend to be broken up into a series of shorter duration events. However, the symbols in Figure 27 seem to be scattered about a similar curve for all three cases, suggesting that a common distribution of hold-up events might apply.

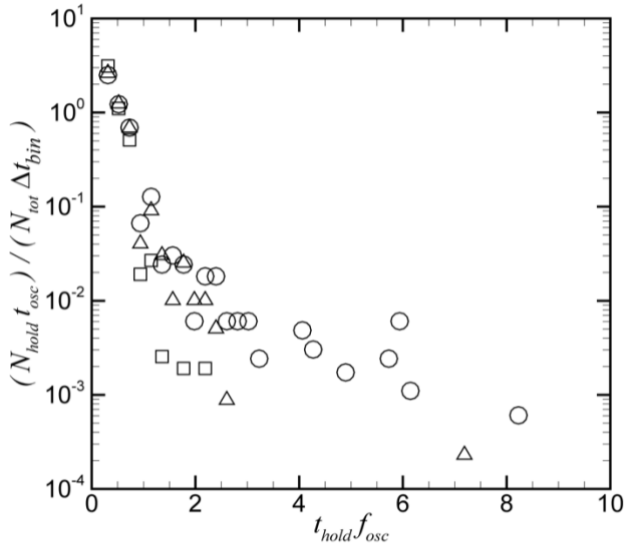

Figure 27: Plot showing the normalized number of hold-up events as a function of the dimensionless hold time $f_{osc} t_{hold}$ for Case B-2 with different values of the cut-off coefficient: $C_{cut} = 0.1$ (squares), 0.2 (deltas), and 0.3 (circles).

In order to characterize the hold-up data, we fit the hold-up distribution plot for each case to a log-normal distribution, with $x \equiv t_{hold} f_{osc}$ treated as a random variable. The fit was done using the following series of steps:

1. The experimental hold-up distribution was integrated in *x* to obtain the cumulative distribution function (C.D.F.), denoted by $F_E(x)$, at the sample points x_i.
2. The log-normal C.D.F., denoted by $F_{LN}(x)$, was fit to the experimental C.D.F. using a least-squares fit, where the resulting pair of nonlinear equations was solved for the coefficients μ and σ using the Newton-Raphson iteration method.
3. The corresponding log-normal probability density function (P.D.F.) $p_{LN}(x)$ was compared to the experimental P.D.F. for hold-up time, which was obtained by plotting $N_{hold}/(N_{tot} f_{osc} \Delta t_{bin})$ versus *x*. The bin width Δt_{bin} in this plot was adjusted to eliminate bins with $N_{hold} = 0$.

In the above, the log-normal P.D.F. and C.D.F. functions are defined by

$$p_{LN}(x) = \frac{1}{x\sigma\sqrt{2\pi}} \exp\left(-\frac{(\ln x - \mu)^2}{2\sigma^2} \right), \tag{23}$$

$$F_{LN}(x) = \frac{1}{2} + \frac{1}{2} \operatorname{erf}\left(\frac{\ln x - \mu}{\sigma\sqrt{2}} \right), \tag{24}$$

where erf(·) denotes the error function.

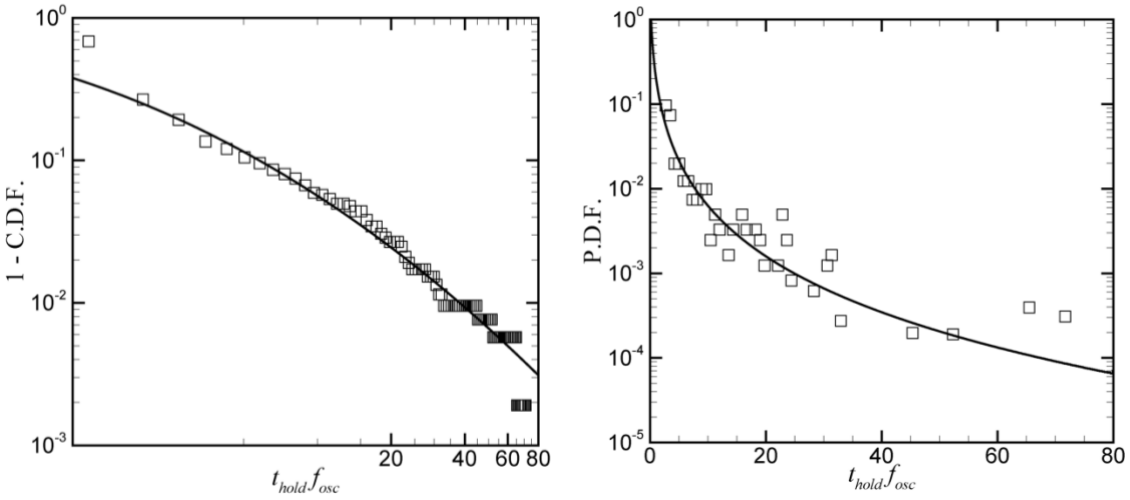

(a) (b)

Figure 28: Example comparing experimental data (symbols) and a log-normal fit (solid line) for (a) the complementary cumulative distribution function (1-C.D.F.) and (b) the probability density function (P.D.F.) for Case B-4.

An example illustrating these steps is given in Figure 28 for Case B-4, where for this case and all further cases discussed in this section we use 150 bins, $C_{cut} = 0.2$, and a bin width of $f_{osc}\Delta t_{bin} = 1$. The log-normal coefficients μ and σ were obtained for each case by a two-step process. In the first step, a square error estimate is defined by

$$E = \sum_{i=1}^{N_{tot}} [F_E(x_i) - F_{LN}(x_i)]^2, \tag{25}$$

where $F_E(x)$ is the experimental cumulative distribution function. The value of E is computed over a grid of μ and σ values with step size 0.01, and the values giving the lowest value of E were identified. In the second step, we obtained a formal least-square error by setting $\partial E / \partial \mu = \partial E / \partial \sigma = 0$, and solved the resulting nonlinear system of

equations with a Newton-Raphson iteration. The μ and σ values obtained from the first step were used as initial guesses for the iteration. The best-fit values of μ and σ for all cases examined are listed in Table 2.

We note that the criterion for hold-up described above will register a hold-up event for a sinusoidally oscillating velocity field each time the velocity passes through zero. These hold-up events are spurious, however, since the particle is not really captured by the porous media, but rather they are simply an artifact of the oscillating velocity field. In order to eliminate these spurious hold-up events from consideration, we do not include hold-up events with $t_{hold} f_{osc} < 0.5$ either in fitting the coefficients μ and σ or in the figures plotting hold-up duration distribution (such as Figure 28). Consequently, the log-normal function should be viewed as a fit to the longer-time hold-up events, but may not be representative of short-time particle hold-up events. The half-period duration for the hold-up time cut-off used here is based on the length of time that the velocity has a given sign during a single oscillation before changing the direction of motion.

The mean value of the log-normal distribution is given by

$$\bar{x}_{LN} = \exp(\mu + \frac{\sigma^2}{2}). \tag{26}$$

This theoretical mean value for log-normal distributions is found to compare reasonably well with the experimental mean value computed directly from the hold-up time distribution, as listed in Table 2, considering that data for long-time hold-up events is fairly sparse. The total percentage of run time that a particle spends in a free state (with $|v| >$

v_{cut}) and in a captured state (with $|v| < v_{cut}$ and $t_{hold} f_{osc} > 0.5$) were computed, as listed in Table 2. The remaining time (not listed in the table) corresponds to time spent by a particle in a captured state with $t_{hold} f_{osc} < 0.5$). For most cases examined, particles were observed to be in a captured state for a very significant percentage of the run time. Also shown in Table 2 is the average frequency of hold-up events, which was computed by the ratio $f_{hold} = N_{tot}/T$ of the total number of hold-up events to the total run time.

Table 2: Data on frequency of particle hold-up and best-fit values of dimensionless μ and σ coefficients from a log-normal distribution to the cumulative distribution function for particle hold-up time.

Run ID	Log-normal coefficients		Mean hold-up time $\bar{t}_{hold}\, f_{osc}$		Percentage time in each state		Hold-up frequency, $f_{hold} t_{osc}$
	μ	σ	Exp.	Log-normal	Free	Capt.	
R-1	-0.125	0.491	0.977	0.996	20.4	47.7	0.489
R-2	-0.121	0.223	0.783	0.908	43.8	9.1	0.116
R-3	0.033	1.314	2.432	2.451	5.1	86.2	0.354
R-4	0.259	1.247	2.691	2.819	5.4	85.0	0.316
R-5	-0.046	0.316	0.935	1.004	14.7	47.3	0.506
R-6	0.044	0.339	1.002	1.107	15.4	46.0	0.459
B-1	-0.387	0.357	0.737	0.724	26.2	17.5	0.237
B-2	-0.086	0.426	0.943	1.005	23.9	23.6	0.250
B-3	-0.392	1.753	3.189	3.141	14.2	56.8	0.178
B-4	-0.557	1.804	2.810	2.916	16.4	41.3	0.147

The cumulative distribution function depends on the particle diameter d and the oscillation frequency f_{osc} and amplitude y_{amp}. A plot of the complementary cumulative distribution function C.C.D.F (= 1 - C.D.F) is shown in Figure 29 for cases with two different particles diameters, $d = 0.52\ mm$ (Case R-4) and $d = 1.3\ mm$ (Case B-4), with the same oscillation frequency and amplitude. The C.C.D.F. values for both particle sizes

are fairly close, with the difference that the larger particles exhibit more long-duration hold-up events and the smaller particle experiences more short-duration hold-up events.

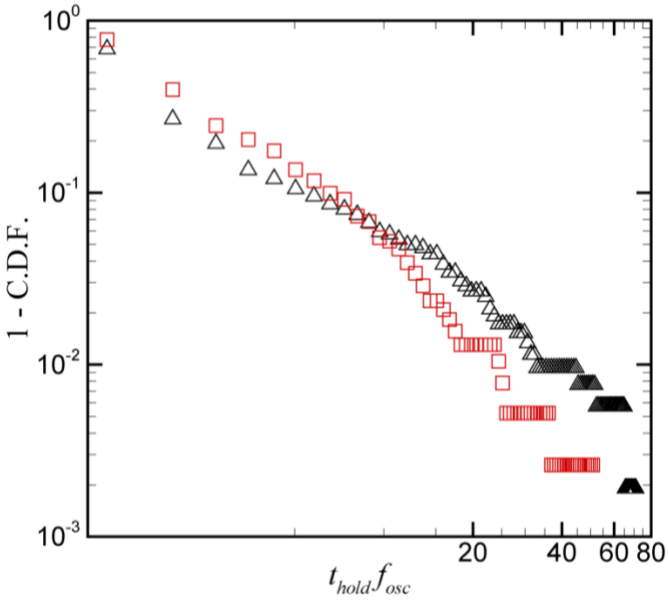

Figure 29: Comparison of complementary cumulative distribution function for cases with particle diameters of $d = 0.52$ mm (red squares, Case R-4) and $d = 1.3$ mm (black deltas, Case B-4).

A comparison of the effect of oscillation frequency on the complementary cumulative distribution function is shown in Figure 30a for Cases B-1 through B-4 with frequency varying from $f_{osc} = 0.15 - 0.75\ Hz$, all having the same oscillation amplitude and particle diameter. A comparison of the effect of oscillation amplitude on the complementary cumulative distribution function is shown in Figure 30b for Cases R-2, R-5 and R-6, with amplitude varying from $y_{amp} = 15.3 - 42.9\ mm$, all having the same oscillation frequency and particle diameter. Comparing these C.C.D.F. plots with the values of run time listed in Table 1, we see that the experimental runs fall into two categories - cases with relatively short run-time and cases with relatively long run-time. The C.C.D.F. is similar for all cases with short run-time (Cases R-1, R-2, B-1, B-2, R-5,

R-6), and it is again similar for all cases with long run-time (Cases R-3, R-4, B-3, B-4); however, the C.C.D.F. for the long run-time cases is shifted significantly to the right of that for the short run-time cases (as soon in Figure 30a). For cases where the run times were relatively short, the longer-duration hold-up events had less of a chance to occur within the experimental time frame than for cases with much longer values of Tf_{osc}, which likely explains the observed difference in the C.C.D.F. plots.

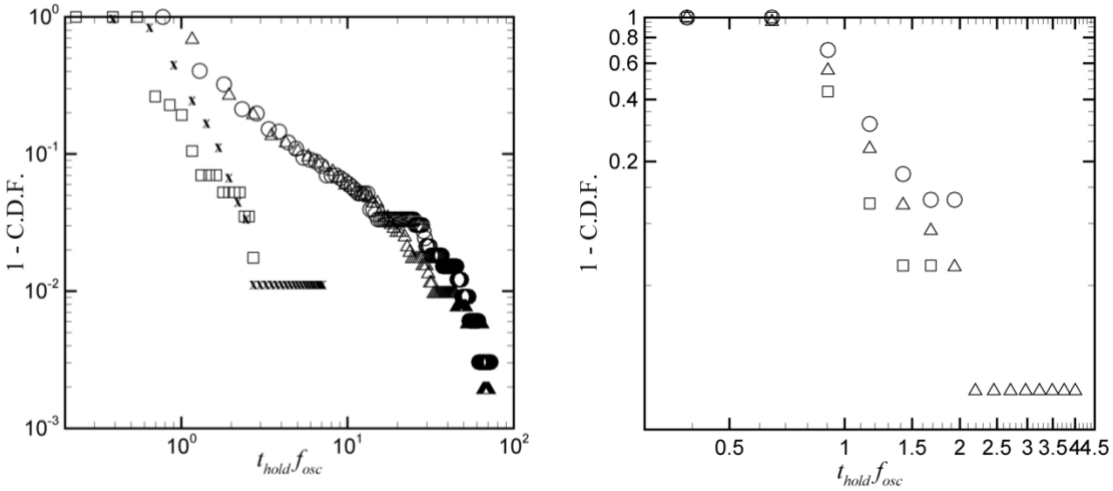

Figure 30: Comparison of complementary cumulative distribution function for cases with (a) oscillation frequency of $f_{osc} = 0.15$ Hz (squares, Case B-1), $f_{osc} = 0.25$ Hz (X's, Case B-2), $f_{osc} = 0.50$ Hz (circles, Case B-3), and $f_{osc} = 0.75$ Hz (deltas, Case B-4) and (b) oscillation amplitude of $y_{amp} = 15.3$ mm (squares, Case R-2), $y_{amp} = 31.0$ mm (deltas, Case R-5), and $y_{amp} = 42.9$ mm (circles, Case R-6).

CHAPTER 6: STOCHASTIC MODEL

Our proposed mechanism to explain oscillatory diffusion involves the notion that a combination of particle oscillation and random hindering yields a diffusion process (Marshall, 2016). For millimeter-scale particles, the hindering occurs primarily via a filtration process, in which particles randomly enter a pore space that is sufficiently small to temporarily trap the particles. When the velocity direction changes, the particle may or may not be able to escape the pore space.

We propose a simple stochastic model in an effort to illustrate the mechanics of the oscillatory diffusion process. In this model, each particle exists in either a free state or a captured state. All particles in the free state move within the porous bed in accordance with (6). The pore size *b* occupied by a particle in the porous bed is treated as a random variable, which is assumed to exhibit a log-normal distribution of the form

$$\boldsymbol{b = b_{min} + d_{bead}\, exp\,(\mu_{pore} + \sigma_{pore} Z)}, \tag{27}$$

The value of $b_{\min}$ is set to the minimum geometrically possible pore size, which is usually associated with the pore space between three touching co-planar spheres whose centers form an equilateral triangle, such that $b_{\min} / d_{bead} = (2\sqrt{3} - 3)/3 \cong 0.155$. In (), Z is a random variable with a standard normal distribution and μ_{pore} and σ_{pore} are adjustable parameters. Plots of the probability density function (P.D.F.) of the pore size difference ratio $(b - b_{\min})/d_{bead}$ are plotted in Figure 31 for different values of the parameters μ_{pore} and σ_{pore}. The value of μ_{pore} is generally negative and the value of σ_{pore} is positive for

the cases examined here, and as the value of μ_{pore} decreases or the value of σ_{pore} increases, the P.D.F. plot exhibits an increasingly large spike for progressively lower values of *Z*. The computations in the current paper were performed with $\mu_{pore} = -1.8$ and $\sigma_{pore} = 1$, which were found to yield a best fit to experimental data for prediction of particle diffusion rate. The P.D.F. plot corresponding to these values of μ_{pore} and σ_{pore} is indicated by a heavy dashed black line in Figure 31.

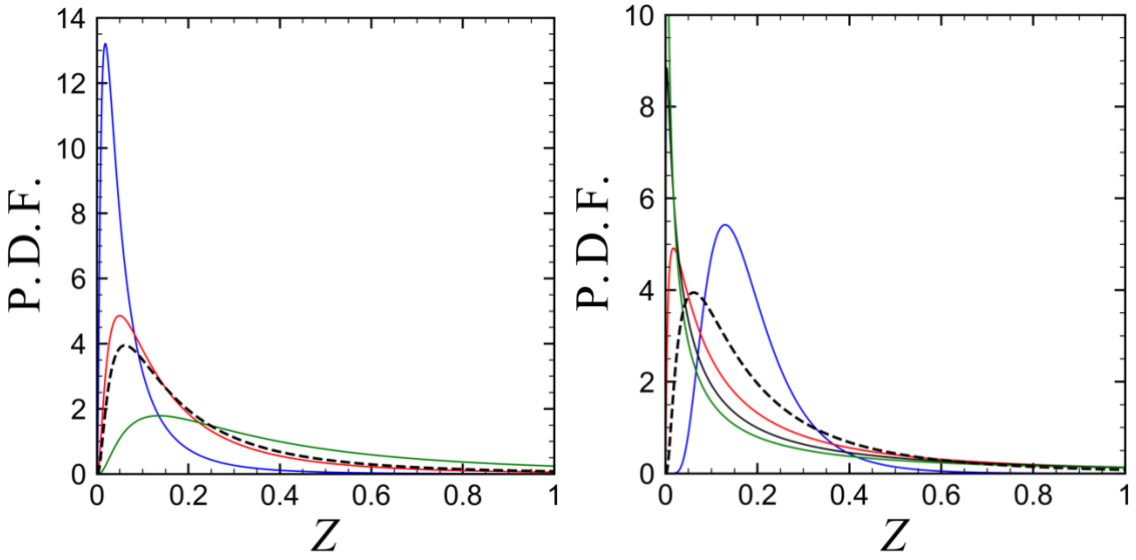

Figure 31: Probability density function (P.D.F.) for the distribution of pore size difference $(b - b_{min})/d_{bead}$ with different values of the parameters μ_{pore} and σ_{pore}: (a) distribution for $\sigma_{pore} = 1$ and $\mu_{pore} = -3$ (A, blue), -2 (B, red), 0 (C, green) and (b) distribution for $\mu_{pore} = -1.8$ and $\sigma_{pore} = 0.5$ (A, blue), 1.5 (B, red), 2.0 (C, green). The dashed black curve is the distribution used for the example computation in the current paper ($\mu_{pore} = -1.8, \sigma_{pore} = 1.0$).

A flow chart of the stochastic model is given in Figure 32. The two possible particle states - free and captured - are indicated using circles. We start with a particle with diameter

d at the circle indicating the free state, in which the particle moves up and down in accordance with the fluid velocity v_f given by

$$v_f(t) = \omega_0 A \sin(\omega_0 t), \tag{28}$$

where A is the nominal oscillation amplitude of a fluid element within the porous bed, $f_{osc} = 1/t_{osc}$ is the flow oscillation frequency, and $\omega_0 \equiv 2\pi f_{osc}$. Each time the particle travels a distance equal to the bead diameter d_{bead}, it enters a new pore space. For each new pore space that the particle enters, there is assumed to be a random process during which the pore size b is selected from the log-normal distribution (27). If the new pore size satisfies the condition $d > b$, then the particle is considered to be captured by the pore. If the pore size fails this condition, then the particle remains in the free state and the cycle will repeat.

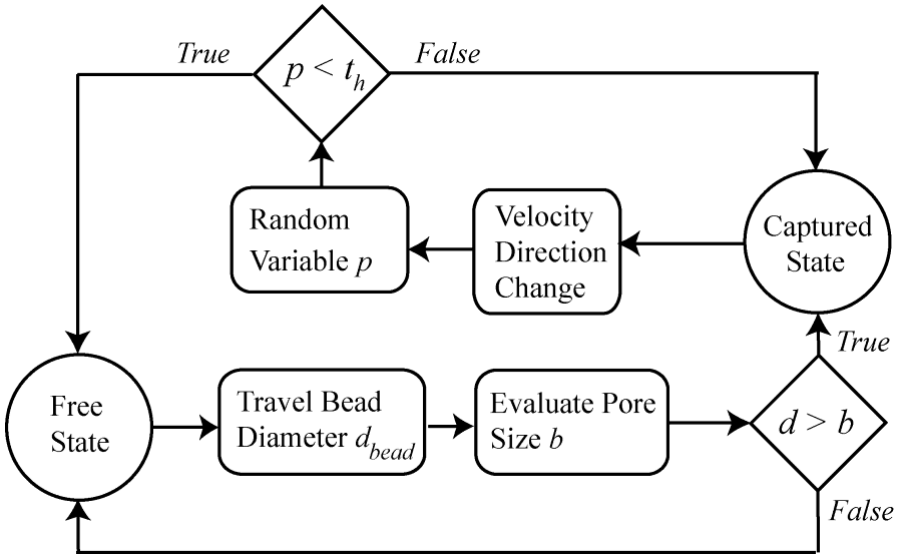

Figure 32: Flow chart of the stochastic model for a particle with diameter d.

A captured particle can be released from the pore when the oscillating fluid velocity v_f changes direction from the value v_{f0} which it had when the particle was captured. However, we observed in our experimental visualizations that captured particles can sometimes bounce around within a pore and remain trapped for multiple cycles of the oscillating flow. Release of a captured particle is therefore represented in the stochastic model via a second probabilistic process, which we call the particle release process. In this release process, at each time step for which $\text{sign}(v_f) \neq \text{sign}(v_{f0})$, we select a random number p with uniform probability distribution between 0 and 1. We also set a prescribed threshold value t_h, such that $0 < t_h < 1$. If the random number p satisfies $p < t_h$, the particle is released from the captured state and reverts back to the free state, so that it again moves with the fluid velocity $v_f(t)$. If the condition $p < t_h$ is not satisfied, then the particle remains in the captured state. In order that the particle behavior is independent of the time step size Δt, we set the value of the threshold as

$$t_h = C_h f_{osc} \Delta t \ , \tag{29}$$

where C_h is a prescribed release coefficient.

To illustrate this stochastic model, an example showing the model predictions was examined for a case with oscillatory flow characterized by $f_{osc} = 0.25$ Hz and $A = 15$ mm and with particle and bead diameters given by $d = 1.3$ mm and $d_{bead} = 6$ mm. The release coefficient for this example calculation is selected as $C_h = 1$. The stochastic model was used to generate an ensemble of 100 data strings, each of which is a different run of the

model with a different initial condition. The runs were conducted with a step size of $\Delta t = 0.03\,\text{s}$, and each run was carried out to an end time of $T = 100\,\text{s}$.

An example trace predicted by a single run of the stochastic model for the particle position $y_p(t)$ and velocity $v_p(t)$ is shown in Figure 33. The value of the velocity alternates between a sinusoidal oscillation (in the free state) and zero (in the captured state). The particle position also alternates between oscillating in time (in the free state) and maintaining a constant value (in the captured state). However, since the time at which this transition occurs is a random variable, the resulting particle motion exhibits a drift in either the upward or downward direction. A set of 20 traces for particles initiated at $y = 0$ are shown in Figure 34a, with some traces ending above and some below the initial location. A probability density function (P.D.F.) of the particle location at dimensionless time $f_{osc}t = 25$ is given in Figure 34b, along with a Gaussian curve characteristic of a typical diffusion process indicated by a solid curve. The two plots in Figure 34 illustrate that oscillatory diffusion behaves like a diffusion process in which the diffusion coefficient is enhanced by the imposed acoustic oscillations.

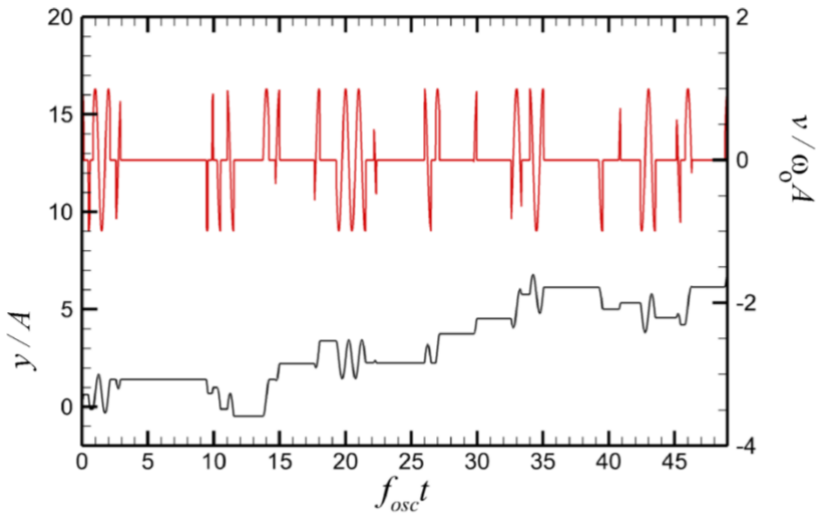

Figure 33: Plot showing time variation of a sample experimental trace for $y_p(t)$ (bottom, left-hand axis) and $v_p(t)$ (top, right-hand axis) for the stochastic model.

.

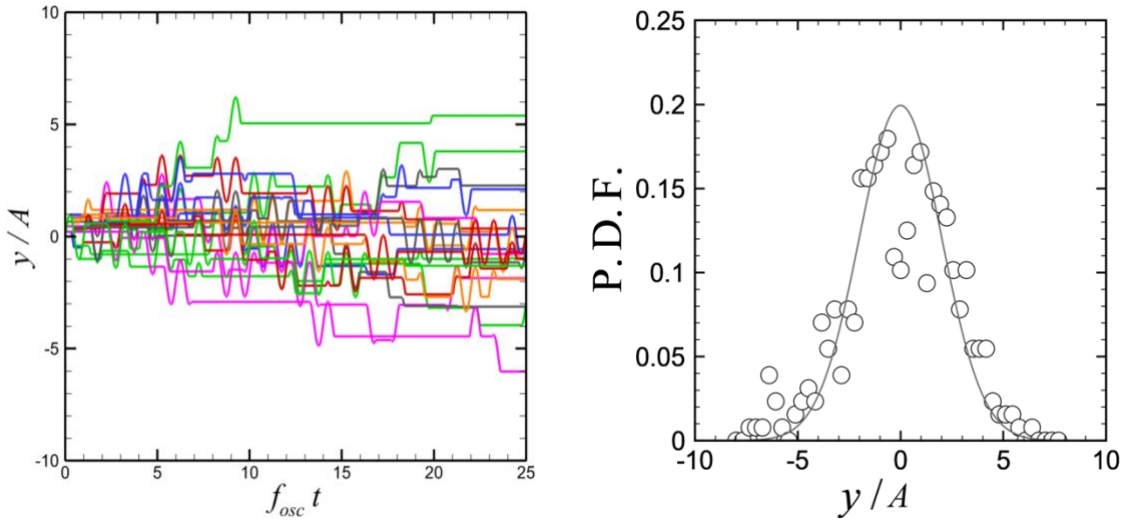

(a) (b)

Figure 34: Illustration of the diffusive characteristic of the particle motion: (a) traces of 20 particles released from $y = 0$, (b) P.D.F. of particle location for 2000 traces sorted into 50 bins in y/A, evaluated at time $f_{osc}t = 25$.

Ensemble-averaged data for the set of 20 data strings are shown in Figure 35a and 35b in comparison to the experimental data for Case B-2. In Figure 35a, the variance is observed to increase in time by fluctuating about a nearly linear increase. A dashed line with the same slope as the linear increase passing through the origin is plotted in Figure 35a. Figure 35b shows the ratio of the kurtosis to the square of the variance for $y(t)$, which after an initial transient oscillates about the theoretical value of 3 for a normally-distributed process (dashed line). The computed autocorrelation for the stochastic model predictions are plotted against the lag time in Figure 35c. The predicted autocorrelation curve is nearly straight, as is also the case for a random walk process. The autocorrelation function for the experimental data in Case B-2 exhibited more oscillation than the stochastic model predictions, but both curves are reasonably close to each other. The power spectrum for the stochastic model predictions is plotted in Figure 35d, with a dashed line representing the $e \propto f^{-2}$ power law on the log-log plot. This power law gives a fairly close fit to the mean slope of the data, as was also the case for the random walk process and the experimental data.

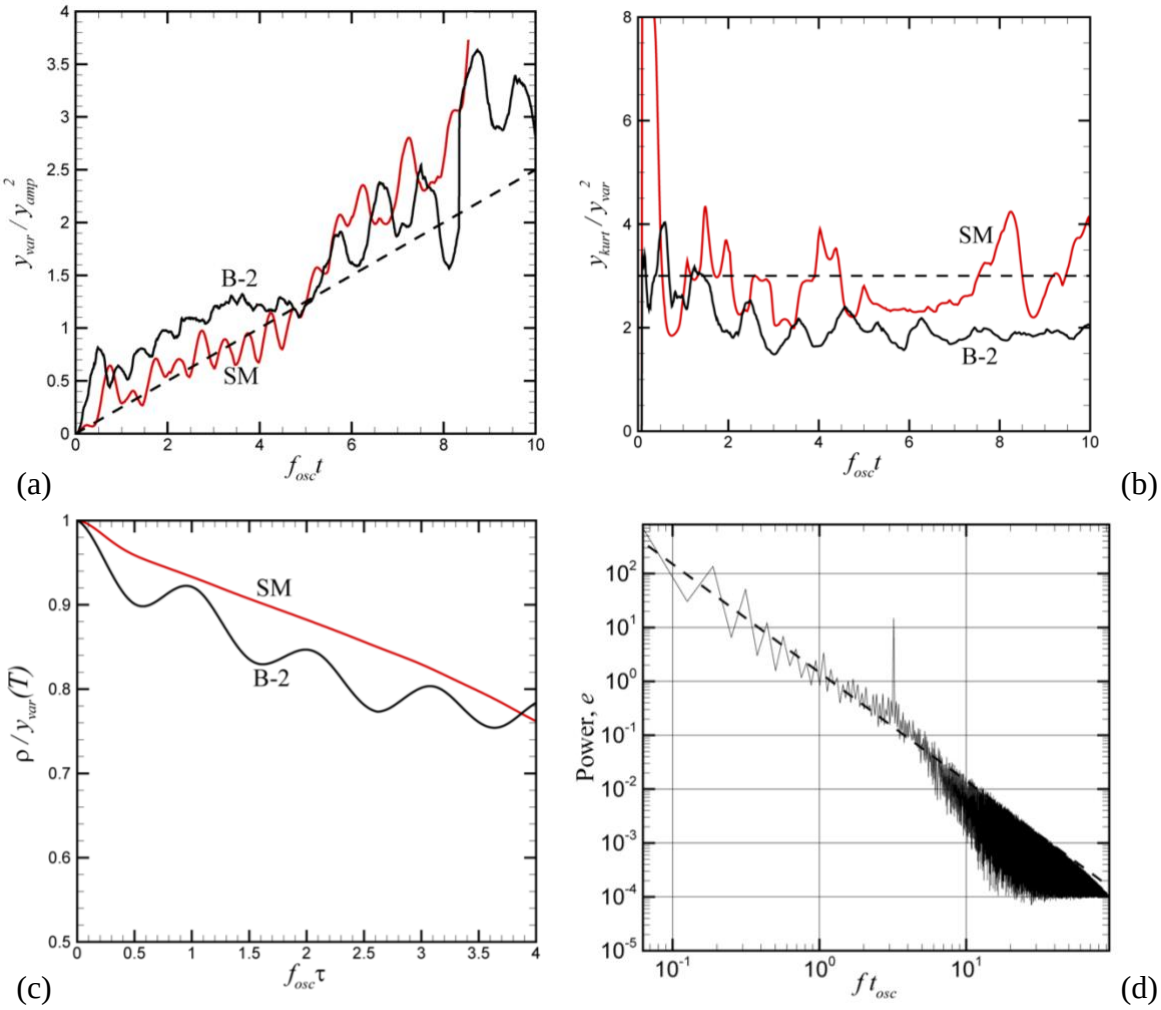

Figure 35: Plots comparing a variety of statistical measures for the experimental case B-2 (B-2, black line I plots a-c) and the stochastic model (SM, red line in plots a-c): (a) the ensemble variance and (b) the ratio of the kurtosis over the variance squared as functions of time; (c) autocorrelation as a function of time delay, and (d) power spectrum for the stochastic model. Dashed lines indicate (a) best fit to slope of variance passing through origin, (b) theoretical value for a normally distributed process, and (d) f^{-2} power law typical of a random walk process.

Hold-up data for the stochastic model predictions is sensitive to the value of the threshold parameter t_h. Smaller values of t_h cause the particles to remain captured for longer times, whereas smaller values of t_h lead to shorter capture times. In Figure 36, the complementary cumulative distribution function and the probability density function are

plotted for the stochastic model predictions with $t_h = 0.017$. The solid lines in these plots represent the best-fit log-normal curves for the experimental data for Case B-2. The stochastic model predictions exhibit more long-duration hold-up events than the experimental log-normal fit. However, even with these differences, the simple probabilistic release model assumed here is nevertheless seen to yield reasonable predictions for distribution of particle hold-up time.

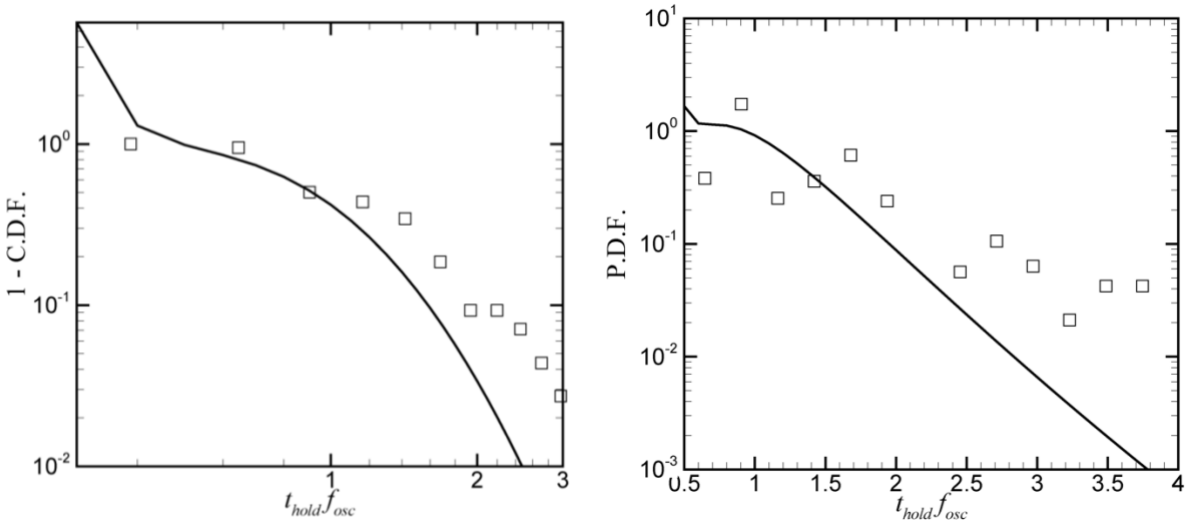

(a) (b)

Figure 36: Plot showing (a) the complementary cumulative distribution function (1-C.D.F.) and (b) the probability density function (P.D.F.), with the stochastic model prediction indicated by symbols and the log-normal fit for the experimental data in Case B-2 indicated by solid lines.

CHAPTER 7: PARAMETRIC STUDY OF STOCHASTIC MODEL AND COMPARISON TO CTRW THEORY

Continuous time random walk (CTRW) is a generalization of the random walk process in which particles wait for a random time increment before jumping between states (Montroll and Weiss, 1965; Balakrishnan and Venkataraman, 1981a). This basic model was generalized by Balakrishnan and Venkataraman (1981b; hereinafter referred to as BV81b) to the problem of *oscillatory diffusion*, where it was assumed that particles fluctuate back and forth between an oscillatory state and a random jump state with constant velocity v_0, and that the transition time between these two states is a random variable. Assuming that the transitions between these states occurs via a series of uncorrelated binary decisions (i.e., a set of Bernoulli trials), BV81b concluded that the holding time distribution for each state would be of the form of a Poisson distribution, which we denote by $p(t)$ for the oscillatory state and by $q(t)$ for the random jump state. In the limit of many state transitions, we assume that these distributions approach the exponential form

$$p(t) = \exp(-tf_{osc} / \tau_0), \qquad q(t) = \exp(-tf_{osc} / \tau_1), \tag{30}$$

where τ_0 and τ_1 are the dimensionless average holding times in the oscillatory and jump states, respectively. The oscillatory diffusion examined in the current paper can be regarded as a special case of that examined in BV81b in which we let the jump velocity $v_0 = 0$, so that the particle is stationary (or captured) in the jump state. We henceforth refer to the jump state of BV81b as the captured state in the current model.

The hold-up time distribution for particle capture in the stochastic model predictions is sensitive to the value of the release coefficient C_h in (29) which is used to determine whether to release a particle or retain it in a captured state. Small values of C_h cause particles to remain captured for longer times than do larger values of C_h. The complementary cumulative distribution function (C.C.D.F.) and the probability density function (P.D.F.) for the hold-up time variable in the captured state are plotted for the example problem with $C_h = 1$ in Figure 37. In this plot, particle capture is identified as occurring for any time step where the absolute value of the particle velocity $v_p(t)$ is less than a fraction C_{cut} of the velocity amplitude $v_{amp} = \omega_0 A$ (22), where $A = y_{amp}$.

For the example case shown in Figure 37, we selected $C_{cut} = 0.1$. The C.C.D.F. data in Figure 37a was fit using the exponential probability distribution (30), which for a semi-logarithmic plot yields a linear expression that passes through the point (0,1) and has slope $-1/\tau_1$. The value of the mean holding-time τ_1 for the captured state was determined using a least-square linear regression to the logarithm of the C.C.D.F., which was selected to give the tails of the distribution equal weight in the fit to the values near the initial time. This procedure yielded an estimate $\tau_1 = 1.82$ with a coefficient of determination of $r^2 = 0.98$, which is indicated by the solid black line in Figure 37. The uncertainty in the estimate of τ_1 is evaluated using a 95% confidence interval, yielding upper and lower bounds for the fit line indicated by the dashed lines in Figure 37.

The C.C.D.F. and P.D.F for the free oscillation time distribution are plotted in Figure 38. The best-fit exponential distribution is indicated in these plots by a solid line, and the 95% confidence interval is indicated by dashed lines. The average holding-time

value for the free oscillation was obtained from the C.C.D.F. data for this example computation as $\tau_0 = 1.44$, with a coefficient of determination of $r^2 = 0.96$.

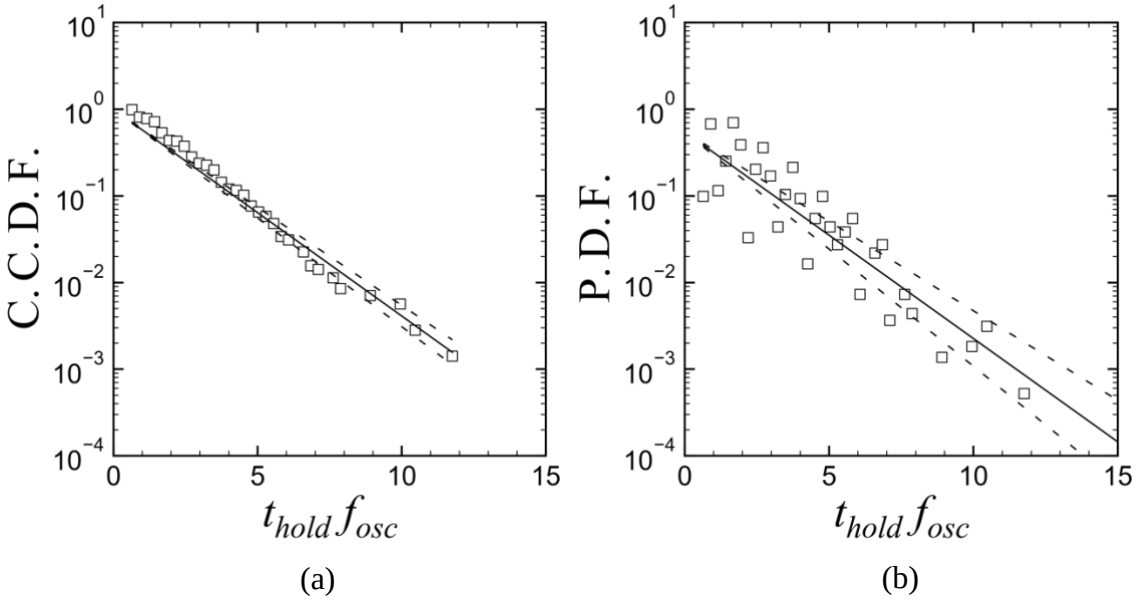

Figure 37: Plots showing results for particle capture-time distribution, including: (a) the complementary cumulative distribution function C.C.D.F. and (b) the probability density function (P.D.F.). The data (symbols) was computed from the stochastic model for the example case described in Chapter 4. The least-square fit (lines) was obtained using the exponential distribution in Eq. (9) with $\tau_1 = 1.82$.

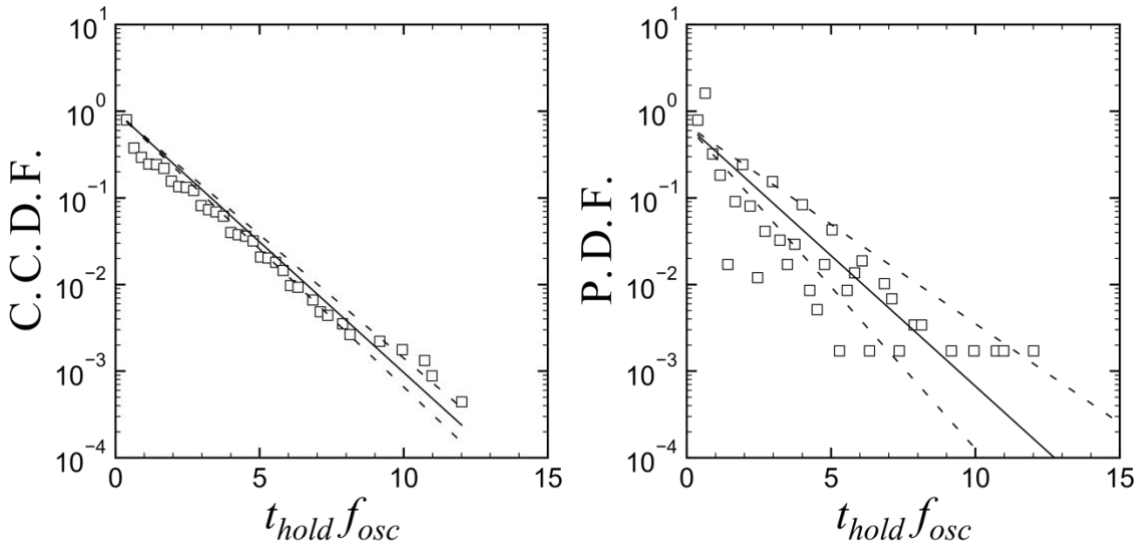

(a) (b)

Figure 38: Plots showing results for free particle oscillation time distribution, including: (a) the complementary cumulative distribution function C.C.D.F. and (b) the probability density function (P.D.F.). The data (symbols) was computed from the stochastic model for the example case described in Chapter 4. The least-square fit (lines) was obtained using the exponential distribution in Eq. (9) with $\tau_0 = 1.44$.

A theoretical expression for the oscillatory contribution to the diffusion coefficient, denoted by D_t, was obtained from the CTRW theory by BV81b, which can be written in terms of the variables used in the current paper as

$$D_T = \frac{A^2 f_{osc}}{2\tau_0}\left[\frac{4\pi^2\tau_0^2}{1+4\pi^2\tau_0^2}\right]. \tag{31}$$

This result indicates that the dimensionless diffusion coefficient, $D_T' \equiv D_T / A^2 f_{osc}$, is a function only of the dimensionless average holding time in the oscillating state, τ_0. The CTRW theory assumes that the particle holding-time has an exponential distribution of the form (30) for both the captured state and the oscillating state, which is in good agreement

with the predictions of our stochastic model (as shown in Figure 37 and Figure 38). However, there are also several differences between our stochastic model assumptions and the CTRW theory. One difference is that the stochastic model only allows the particle to become captured after it has traveled a distance equal to the bead diameter, whereas the CTRW theory has no minimum travel distance for transition of the particle state. Secondly, the stochastic model only allows particle release from a captured state during times where the velocity is opposite in sign to that at which the capture occurred. No such restriction is found in the CTRW theory.

A parametric study was conducted to test sensitivity of the stochastic model to various physical and numerical parameters, and to compare predicted diffusion coefficient values with those of the CTRW theory. The numerical parameters examined include the dimensionless time step $\Delta t' = f_{osc}\Delta t$, the velocity cut-off coefficient C_{cut} used in (22) for assigning a particle to a captured state, and the particle release coefficient C_h in (29). The physical parameters examined include the ratio of oscillation amplitude to bead diameter A/d_{bead}, the ratio of particle diameter to bead diameter d/d_{bead}, and the pore size parameter σ_{pore}. The dimensionless diffusion coefficient D_S' from the stochastic model was computed for each case using the variance data from the model as

$$D_S' = \frac{1}{2}\frac{dy'_{\mathrm{var}}}{dt'}. \tag{32}$$

where $y'_{van} = y_{\mathrm{var}} / A^2$ and $t' = f_{osc} t$ are the dimensionless variance and time, respectively. The derivative in (32) was obtained using a linear fit to the variance data obtained by linear regression. The comparison theoretical value of the dimensionless diffusion coefficient from CTRW theory, D'_T, was calculated using (31) with the average holding time τ_0 for the free oscillation state extracted from the stochastic model data using a least-square fit of the exponential C.C.D.F. distribution, as shown in Figure 38.

It is noted that the stochastic model is dependent on the values of a series of random numbers, and as a consequence the predicted values of the dimensionless diffusion coefficient obtained from the stochastic model, D'_S, are not the same for two repeated runs of the code, even if all parameter values are the same. We also observe variation between runs for the value of τ_0, which therefore results in fluctuations in the theoretical prediction for D'_T from (31). In order to quantify the size of the fluctuations in diffusion coefficient values, we performed two sets of experiments by repeated runs for a 'standard case', for which the dimensionless parameter values are given as follows:

$$C_{cut} = 0.1, \qquad C_h = 1, \qquad \Delta t' = 0.0083, \qquad A / d_{bead} = 2.55,$$

$$d / d_{bead} = 0.217, \qquad b_{\min} / d_{bead} = 0.155, \quad \sigma_{pore} = 1, \qquad \mu_{pore} = -1.8. \qquad (33)$$

which is consistent with the example case described in Chapter 4. The stochastic model computation was repeated for these parameter values both 20 times and 100 times. The mean and standard deviation of the predicted values of D'_S and D'_T for each of these sets of runs are recorded in Table 3. The standard deviation of the stochastic model prediction

is between 10-12% of the mean value, whereas that of the CTRW theory prediction is between 1-3% of the mean value. Comparison of the mean and standard deviation values for the cases with 20 and 100 iterations indicates the sensitivity of these values to number of iterations.

Table 3: Comparison of the mean and standard deviation of the predictions for dimensionless diffusion coefficient from the stochastic model and the CTRW theory for different number of iterations of the model.

Quantity	20 Iterations		100 Iterations	
	mean	standard deviation	mean	standard deviation
Stochastic model, D_S'	0.1467	0.0153	0.1523	0.0176
CTRW theory, D_T'	0.1562	0.00405	0.1541	0.00219

In the parametric study, we examine sensitivity of the stochastic model predictions to variation of the first six parameters listed in (33). For each parameter, 20 different values were examined by varying the test parameter value while holding the remaining parameters constant. Each run was repeated 100 times to obtain mean and standard deviation for each set of parameter values. Plots showing the predictions for dimensionless diffusion coefficient from both the stochastic model and the CTRW theory are shown in Figure 39 for the three stochastic model numerical parameters, C_{cut}, C_h, and $\Delta t'$. In Figure 40, dimensionless diffusion coefficient predictions from the CTRW theory and the stochastic model are presented for three physical parameters describing the porous bed, the oscillating flow, and the moving particle. The mean value is indicated in these plots by a symbol and the standard deviation is indicated by error bars.

Figure 39a shows that the predicted diffusion coefficient values from the stochastic model and the CTRW theory agree well under the standard model conditions listed in (33), and that neither of these predicted diffusion coefficient values change significantly as the value of C_{cut} is varied from 0 - 0.4. We recall that C_{cut} is used in the criterion (22) to determine when a particle transitions from a free state to a captured state in the stochastic model. The reported results indicate that the model predictions are not sensitive to the value of this velocity cut-off coefficient.

The second numerical parameter examined was the dimensionless time step $\Delta t'$. Sensitivity of predicted diffusion coefficient to $\Delta t'$ is examined in Figure 39b, which shows that both the CTRW theory and the stochastic model predictions have little sensitivity to this parameter when $\Delta t'$ is greater than about 0.005. However, for computations with $\Delta t'$ much smaller than this value, the stochastic model predictions exhibit a small increase in diffusion coefficient while the CTRW theory exhibits a very large increase. The difference between the CTRW predictions and the stochastic model predictions for small values of $\Delta t'$ is associated with the fact that the stochastic model is only allowed to make a decision for whether or not a particle is captured after the particle has traveled a distance equal to a multiple of the bead diameter, whereas the CTRW theory makes this decision at every time step. The ratio of distance traveled by the particle to bead diameter can be estimated using the velocity amplitude $\omega_0 A$ from (28) for the maximum velocity as

$$\frac{\Delta y}{d_{bead}} = \frac{V}{f_{osc} d_{bead}} \Delta t' = O(2\pi \Delta t' \frac{A}{d_{bead}}). \tag{34}$$

In terms of this parameter, breakdown in agreement between the stochastic model and the CTRW theory coincides in Figure 39b with the condition

$$\Delta t' \frac{A}{d_{bead}} < 0.015 . \tag{35}$$

The final numerical parameter examined was the particle release coefficient C_h, which is used in the expression (29) to determine the value of the release threshold t_h used to determine if a particle is released from a captured state. The results in Figure 39c indicate that the CTRW theory predicts a nearly linear increase in the diffusion coefficient with C_h. The CTRW theoretical prediction agrees closely with the stochastic model prediction for $C_h < 1.8$, but above this value the stochastic model prediction begins to flatten out. These results indicate that C_h is the primary numerical parameter that influences the predictions of the stochastic model.

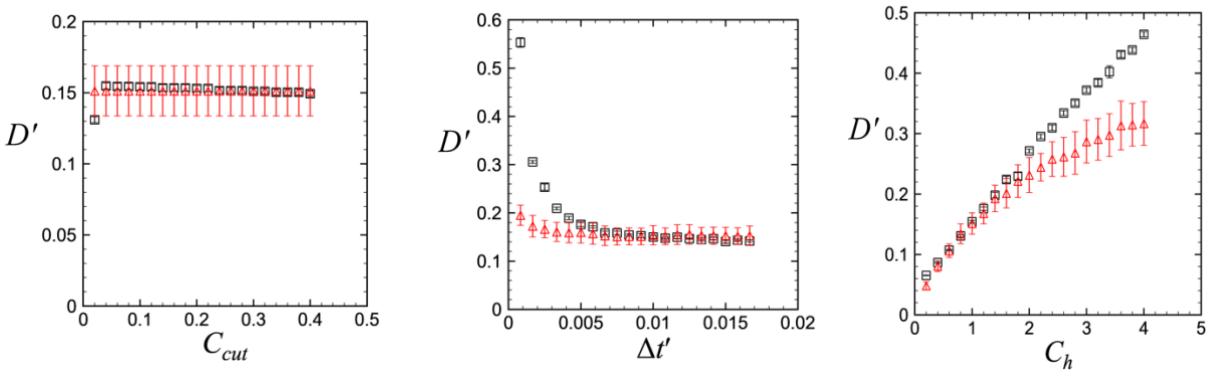

(a) (b) (c)

Figure 39: Sensitivity study of the dimensionless diffusion coefficient predictions for the stochastic model (red triangles) and the CTRW theory (black squares) as functions of three different numerical parameters: (a) C_{cut}, (b) $\Delta t'$, and (c) C_h. Symbols represent the mean value and error bars represent the standard deviation of 100 repeated computations for each point.

It would be expected that physical parameters, such as the particle and bead diameters, the frequency and amplitude of oscillation, and the pore size distribution of the underlying porous medium, would influence the resulting particle diffusion. From these variables, we selected three dimensionless physical parameters to examine sensitivity of the predicted dimensionless diffusion coefficient. The first parameter, A/d_{bead}, represents the ratio of the maximum amplitude of particle displacement to the bead diameter. Based on the criterion (35) with the dimensionless time step given in (33), we would expect the stochastic model predictions to begin deviating from the CTRW theory for $A/d_{bead} < 1.8$, which agrees well with the results in Figure 40a. Because the particle can only change from a freely oscillating state to a captured state in the stochastic model if it travels a distance greater than d_{bead}, the diffusion coefficient predicted by the stochastic model, shown in Figure 40a, reduces to zero when the maximum distance of particle displacement ($2A$) is less than d_{bead} (or $A/d_{bead} < 1/2$).

The stochastic model predictions are highly sensitive to the value of the ratio d/d_{bead} of the particle diameter to the bead diameter. If $d/d_{bead} < b_{min}/d_{bead} = 0.155$, the particles will always be smaller than the pore size and pass through the pore without hold-up, with the consequence that the diffusion coefficient will vanish. We note that the current stochastic model is based on the assumption that particle capture occurs only from filtration, and it does not include effects of particle adhesion or other forms of hindering. On the other hand, as d/d_{bead} gets large, the likelihood of the particle encountering a pore that is smaller than the particle becomes progressively smaller. This results in a condition where the particle becomes continually captured by the surrounding beads, with rapid decrease in diffusion coefficient. As a result of these two considerations, we see in Figure

40b that the diffusion coefficient predicted by the stochastic model has a fairly narrow peak and reduces rapidly when d/d_{bead} is either larger or smaller than this peak value. The location of the peak value and the narrowness of the profile will be dependent primarily on the parameters μ_{pore} and σ_{pore} that govern the assumed pore size distribution. In the region with highest diffusion coefficient value within this peak region, the CTRW theory predictions are close to those of the stochastic model; however, the CTRW theory does not provide an accurate prediction for values of d/d_{bead} outside of this peak region.

The final physical parameter examined is σ_{pore}, which as shown in Figure 31 influences the shape of the pore size distribution. The diffusion coefficient predictions for computations with different values of σ_{pore} is shown in Figure 40c. For small values of σ_{pore}, the pore size distribution has a very narrow peak, and hence only a narrow range of d/d_{bead} values exhibit significant diffusion. As σ_{pore} increases, the pore size distribution widens, and significant diffusion coefficient values are observed for a larger interval of d/d_{bead} values. For the value of d/d_{bead} listed in (34) we observe a significant decrease in the diffusion coefficient predicted by the stochastic model for σ_{pore} less than about 0.9. For values of σ_{pore} above this value, the diffusion coefficient exhibits small sensitivity to σ_{pore} and the predictions of CTRW theory and of the stochastic model are reasonably close.

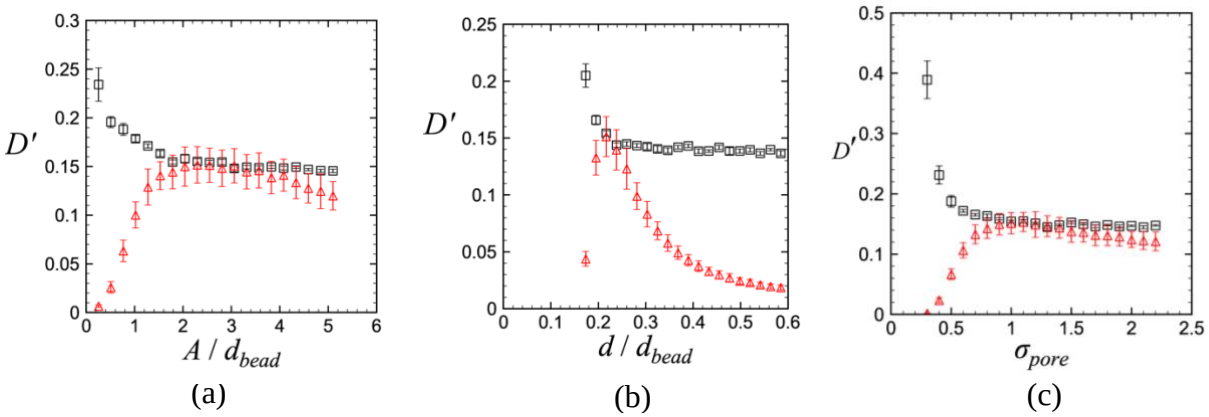

Figure 40: Parametric study of the dimensionless diffusion coefficient predictions for the stochastic model (red triangles) and the CTRW theory (black squares) as functions of three physical parameters: (a) A/d_{bead}, (b) d/d_{bead}, and (c) σ_{pore}. Symbols represent the mean value and error bars represent the standard deviation of 100 repeated computations for each point.

CHAPTER 8: CONCLUSIONS

A study has been performed on the effect of oscillatory forcing on the enhancement of diffusion of colloidal particles suspended in a rigid porous bed composed of fixed spheres. The combination of particle oscillation induced by the oscillatory flow and random hindering due to interaction with the porous bed produces a type of particle random walk. This combination leads to particle diffusion in the bed via a process known as oscillatory diffusion. This process was studied experimentally by following individual particles moving under an imposed oscillatory flow field in a porous bed of spherical glass beads. Refractive index matching was used to visualize the particle in the porous bed. The particle was observed to oscillate up and down with the imposed oscillatory flow field, but also to intermittently be captured by the porous bed for intervals of various durations. The particle location data was extracted from video images, from which the particle position and velocity were determined as functions of time. Experiments were conducted with two different particle sizes and with various frequencies and amplitudes of the oscillating flow field. Each condition was repeated approximately 20 times to generate an ensemble of data.

A variety of statistical measures were applied to the experimental data for particle position within the porous bed in the presence of oscillatory flow, including ensemble averaging, autocorrelation, spectral analysis, and distribution of particle hold-up times. These measures were found to exhibit many attributes similar to diffusive processes, including nearly linear increase in variance with time, nearly linear decrease in autocorrelation as a function of lag time, and a power-law dependence $e \propto f^{-2}$ between spectral power and frequency. At the same time, the experimental data also exhibited some attributes of an oscillatory process, which resulted in superposition of oscillations for the

variance and autocorrelation functions onto the linear dependence typical of diffusive processes. The distribution of particle hold-up duration that characterizes the intermittent particle capturing was found to be well fit by a log-normal distribution. The cumulative distribution plots were used to compare the hold-up distribution data for the different cases examined.

A stochastic model was developed to describe the oscillatory diffusion process for particles in a porous bed which involves a transition between a freely oscillating state and a captured state of the particle. A particle that is initially freely oscillating can become captured if it moves into a pore space that is smaller than the particle diameter, where the pore size is assumed to be a log-normally distributed random variable. However, the particle only moves into a new pore space once it has moved a distance equal to the nominal diameter of the beads making up the porous bed, which places a limit of the frequency that particle state transition can occur. Once a particle is captured, it can transition back to the freely oscillating state during the particle release process, which occurs only when the sign of the velocity is opposite that at which the initial capture occurred. Particle release is allowed to occur when the value of a uniformly-distributed random variable is less than a threshold value. Example computations using this stochastic model exhibit many of the theoretical characteristics of random walk processes such as a linearly increasing variance, a ratio of kurtosis to square of variance close to 3.0, and a power spectrum that is inversely proportional to the square of the frequency. The hold-up time for both the capture and freely-oscillating states are found to be well fit by exponential probability distributions in the stochastic model.

The oscillatory diffusion process was described in terms of a continuous time random walk (CTRW) process by Balakrishnan and Venkataraman (1981b) and includes an analytical solution for the particle diffusion coefficient; however, some of the assumptions made in development of this CTRW theory are not consistent with the physical processes involved for particles in a porous bed. After being non-dimensionalized by $A^2 f_{osc}$, where A is the particle oscillation amplitude in the porous bed and f_{osc} is the oscillation frequency, the dimensionless diffusion coefficient was found to depend only on the dimensionless particle average hold-up time τ_0 in the freely oscillating state. A parametric study of the sensitivity of the stochastic model was performed by varying three dimensionless numerical parameters that control the stochastic model and three dimensionless physical parameters describing properties of the particle, the porous bed, and the acoustic forcing. For each case the dimensionless diffusion coefficient predicted by the stochastic model was compared with the analytical solution from the CTRW theory. The degree of sensitivity of the stochastic to different parameters was determined, and regions exhibiting agreement and disagreement of the stochastic model predictions with the CTRW theory were identified and explained.

We caution that the current experiments and stochastic model are limited to particulate transport at the millimeter size scale. For much smaller-scale processes, such as the problem of ultrasound-enhanced diffusion of nanoparticles in a hydrogel, other processes come into play. For instance, for small-scale particles, adhesive capture of the particles by the hydrogel network is expected to be an important hindering mechanism. The stochastic model also assumed that the particle was either moving freely or at rest and

did not account for an in-between state in which the surrounding porous media slows down (but does not stop) the particle motion.

REFERENCES

Balakrishnan, V., Venkataraman, G., Two-state random walk model of diffusion. 2. Oscillatory diffusion. Pramana 16(6), 437-455 (1981b).

Bigelow, T.A., Northagen, Y.T., Hill, T.M., Saileret, F.C., The destruction of escherichia coli biofilms using high-intensity focused ultrasound, Ultrasound in Med. & Biol 35(6), 1026–1031, (2009)

Bsoul, A.A., Magnin, J.P., Commenges-Bernole, N., Gondrexon, N., Willison, J., Petrier, Christian., Effectiveness of ultrasound for the destruction of Mycobacterium sp. strain (6PY1), Ultrasonics Sonochemistry 17, 106–110 (2010)

Bertrand, N., Leroux, J.C., The journey of a drug-carrier in the body: An anatomo-physiological perspective, Journal of Controlled Release (2011).

Bae, Y.H., Park, K., Targeted drug delivery to tumors: myths, reality and possibility, J Control Release 153(3), 198–205 (2011).

Bradford S.A., Yates, S.R., Bettahar, M., Simunek, J., Physical factors affecting the transport and fate of colloids in saturated porous media, Water Resources Research 38(12), 1321 (2002)

Bradford, S.A., Simunek, J., Bettahar, M., Van Genuchten, M.T., Yates, S.R., Modeling Colloid Attachment, Straining, and Exclusion in Saturated Porous Media, Environ. Sci. Techno 37, 2242-2250 (2003).

Bradford S.A., Simunek, J., Bettahar, M., van Genuchten, M.T., Yates, S.R., Significance of straining in colloid deposition: Evidence and implications, Water Resour. Res., 42, W12S15, doi:10.1029/2005WR004791 (2006).

Braeckmans, K., Probing the size limit for nanomedicine penetration into Burkholderia multivorans and Pseudomonas aeruginosa biofilms. Journal of Controlled Release 195, 21-28 (2014a).

Beuling, E.E., van Dusschoten, D., Lens, P., van den Heuvel, J.C., Van As, H., Ottengraf, S.P.P., Characterization of the diffusive properties of biofilms using pulsed field gradient-nuclear magnetic resonance, Biotechnology and Bioengineering 60(3), (1998).

Cheow, W.S., Chang, M.W., Hadinoto, K., The roles of lipid in anti-biofilm efficacy of lipid-polymer hybrid nanoparticles encapsulating antibiotics. Colloids and Surfaces A: Physicochemical and Engineering Aspects 389, 158-165 (2011).

Corradini, F., Meza, P., Eguiluz, R., Casado, F., Huerta-Lwanga, E., Geissen, V., Evidence of microplastic accumulation in agricultural soils from sewage sludge disposal, Science of the Total Environment 671, 411–420 (2019).

Chernomordik, V., Gandjbakhchea, A.H., Hassana, M., Pajevicb, S., Weissb, G.H., A CTRW-based model of time-resolved fluorescence lifetime imaging in a turbid medium, Opt Commun. 283(23), 4832–4839 (2010)

Dieterich, W., Peschel, I., Schneider, W.R., Diffusion in periodic potentials, Z. Physik 27, 177 -187 (1977).

Das, A.K., Stochastic diffusion in a periodic potential, Physica 98A, 528-544 (1979).

David, J., Weissmannova, H.D., Steinmetz, Z., Kabelikova, L., Demyan, M.S., Simeckova, J., Tokarski, D., Siewert, C., Schaumann, G.E., Kucerik, J., Introducing a soil universal model method (SUMM) and its application for qualitative and quantitative determination of poly(ethylene), poly(styrene), poly(vinyl chloride) and poly(ethylene terephthalate) microplastics in a model soil, Chemosphere 225, 810e819 (2019).

Fatin-Rouge, N., Starchev, K., Buffle, J., Size effects on diffusion processes within agarose gels, Biophysical Journal Volume 86, 2710–2719 (2004)

Forier, K., Messiaen, A.S., Raemdonck, K., Nelis, H., De Smedt, S., Demeester, J., Coenye, T., and Braeckmans, K., Probing the size limit for nanomedicine penetration into Burkholderia multivorans and Pseudomonas aeruginosa biofilms. Journal of Controlled Release 195, 21-28 (2014a).

Forier, K., Messiaen, A.S., Raemdonck, K., Nelis, H., De Smedt, S., Demeester, J., Coenye, T., Braeckmans, K., Probing the size limit for nanomedicine penetration into Burkholderia multivorans and Pseudomonas aeruginosa biofilms. Journal of Controlled Release 195, 21-28 (2014a)

Forier, K., Raemdonck, K., De Smedt, S.C., Demeester, J., Coenye, T., Braeckmans, K., Lipid and polymer nanoparticles for drug delivery to bacterial biofilms. Journal of Controlled Release 190, 607-623 (2014b).

Fu, W., Min, J., Jiang, W., Li, Y., Zhang, W., Separation, characterization and identification of microplastics and nanoplastics in the environment, Science of the Total Environment 721, 137561 (2020).

Gerber, G., Rodts, S., Aimedieu, P., Faure, P., Coussot, P., Particle-size exclusion clogging regimes in porous media, Physcal Review Letters 120, 148001 (2018)

Hahn M.W., O'Melia, C.R., Deposition and reentrainment of brownian particles in porous media under unfavorable chemical conditions: some concepts and applications, Environ. Sci. Technol. 38, 210-220 (2004)

Hunter, P., The mob response: the importance of biofilm research for combating chronic diseases and tackling contamination, EMBO reports 9(4), (2008).

Huffer T., Metzelder, F., Sigmund, G., Slawek, S., Schmidt, T.C., Hofmann, T., Polyethylene microplastics influence the transport of organic contaminants in soil, Science of the Total Environment 657, 242–247 (2019).

Kermani, M.S., Jafari, S., Rahnama, M., Raoof, A., Direct pore scale numerical simulation
of colloid transport and retention. Part I: Fluid flow velocity, colloid size, and pore structure effects, Advances in Water Resources 144, 103694 (2020).

Kuzmina, L., Osipov, T., Deep bed filtration with multiple pore-blocking mechanisms. Theoretical Foundation of Civil Engineering 196, 04003 (2018).

King, L.V., On the acoustic radiation pressure on spheres, The Royal Society 147(861), (1934).

Kim, S.W., An, Y.J., Soil microplastics inhibit the movement of springtail species, Environment International 126, 699–706 (2019).

Kokare, C.R., Charkraborty, S., Khopade, A.N., Mahadik, K.R., Biofilm: importance and applications, Indian Journal of Biotechnology 8, 159-168 (2008).

Laspidou, C.S., Spyrou, L.A., Aravas, N., Rittmann, B.E., Material modeling of biofilm mechanical properties, Mathematical Biosciences 251, 11–15 (2014).

Lee-Haung, L., Adhesive Bonding, Springer Science+Business Media New York, DOI 10.1007/978-1-4757-9006-1 (1991)

Li, X., Yeh, Y.C., Giri, K., Mout, R., Landis, R.F., Prakash, Y.S., and Rotello, V.M., Control of nanoparticle penetration into biofilms through surface design. Chem. Commun. 51, 282-285 (2015).

Ma, D., Green, A.M., Willsey, G.G., Marshall, J.S., Wargo, M.J., and Wu, J.R., Effects of acoustic streaming from moderate-intensity pulsed ultrasound for enhancing biofilm mitigation effectiveness of drug-loaded liposomes. Journal of the Acoustical Society of America 138(2), 1043-1051 (2015).

Ma, D., Marshall, J.S., and Wu, J.R., Measurement of ultrasound-enhanced diffusion coefficient of nanoparticles in an agarose hydrogel. Journal of the Acoustical Society of America 144(6), 3496-3502 (2018).

Masoliver, J., Montero, M., Perello, J., Weiss, G.H., The CTRW in finance: Direct and inverse problems with some generalizations and extensions, Physica A 379, 151–167 (2006)

Miller, J.K., Neubig, R., Clemons, C.B., Kreider, K.L., Wilber, J.P., Young, G.W., Ditto, A.J., Yun, Y.H., Milsted, A., Badawy, H.T., Panzner, M.J., Youngs, W.J., Cannon, C.L., Nanoparticle deposition onto biofilms, Ann Biomed Eng. 41(1), 53–67, doi:10.1007/s10439-012-0626-0 (2013).

Marshall, J.S., A model of ultrasound-enhanced diffusion in a biofilm. Journal of the Acoustical Society of America 139(6), EL228-EL233 (2016).

Machado, A.A.S., Lau, C.W., Kloas, W., Bergmann, J., Bachelier, J.B., Faltin, E., Becker, R., Gorlich, A.S., Rillig, M.C., Microplastics can change soil properties and affect plant
Performance, Environ. Sci. Technol. 53, 6044−6052 (2019).

Oliveira, F.A., Ferreira, R.M.S., Lapa, L.C., Vainstein, M.H., Anomalous diffusion: a basic mechanism for the evolution of inhomogeneous systems, Frontiers in Physics 7(18), (2019).

Porubcan A.A., Xu, S., Colloid straining within saturated heterogeneous porous Media, Water Research 45, 1796-1806 (2011).

Pizzi, A., Mittal, K.L., Handbook of adhesive technology second edition, revised and expanded, Marcel Dekker, Inc, ISBN: 0-8247-0986-1 (2003)

Peulen, T.O., and Wilkinson, K.J., Diffusion of nanoparticles in a biofilm. Environmental Science
& Technology 45, 3367-3373 (2011).

Paul, S., Nahire, R., Mallik, S., Sarkar, K., Encapsulated microbubbles and echogenic liposomes for contrast ultrasound imaging and targeted drug delivery, Comput Mech 53, 413–435 (2014).

Paul, S., Nahire, R., Mallik, S., Sarkar, K., Encapsulated microbubbles and achogenic liposomes for contrast ultrasound imaging and targeted drug delivery. Computational Mechanics 53, 413-436 (2014).

Piti, W.G., Mcbride, M.O., Lunceford, J.K. , Roper, R.J., Sagers, R.D., Ultrasonic enhancement of antibiotic action on gram-negative bacteria, Antimicrobial Agents And Chemotherapy 38(11), 2577-2582 (1994).

Pitt, W.G., Husseini, G.A., Staples, B.J., Ultrasonic drug delivery – a general review, Expert Opin Drug Deliv. 1(1), 37–56 (2004)

Qian, Z., Stoodley, P., Pitt, W.G., Effect of low-intensity ultrasound upon biofilm structure from confocal scanning laser microscopy observation, Biomaterials 17, 1975-1980 (1996).

Qian, Z., Sagers, R.D., Pitt, W.G., The effect of ultrasonic frequency upon enhanced killing of
p. aeruginosa biofilms, Annals of Biomedical Engineering 25, 69-76 (1997)

Rediske, A.M., Roeder, B.L., Brown, M.K., Nelson, J.L., Robison, R.L., Draper, D.O., Schaalje, G.B., Robison, R.A., Pitt, W.G., Ultrasonic enhancement of antibiotic action on escherichia coli biofilms: an in vivo model, Antimicrobial Agents And Chemotherapy 43(5), 1211–121 (1999)

Rillig, M.C., Microplastic in terrestrial ecosystems and the soil?, American Chemical Society 2012.

Rillig , M.C., Ziersch, L., Hempel, S., Microplastic transport in soil by earthworms, Scientific Reports 7, 1362, DOI:10.1038/s41598-017-01594-7 (2017)

Singh, R., Lillard, J.W., Nanoparticle-based targeted drug delivery, Exp Mol Pathol. 86(3), 215–223. doi:10.1016/j.yexmp.2008.12.004. (2009)

Schroeder, A., Kost, J., Barenholz, Y., Ultrasound, liposomes, and drug delivery: principles for using ultrasound to control the release of drugs from liposomes. Chemistry and Physics of Lipids 162, 1-16 (2009).

Sirivithayapakorn, S., Keller, A., Transport of colloids in saturated porous media: A pore-scale observation of the size exclusion effect and colloid acceleration, Water Resources Research 39(4), 1109 (2003).

Seetha, N.,Hassanizadeh, S.M.,Mohan Kumar, M. S., Raoof, A., Correlation equations for average deposition rate coefficients of nanoparticles in a cylindrical pore, Water Resour. Res., 51, 8034–8059, doi:10.1002/2015WR017723 (2015).

Shen, C., Li, B., Haung, Y., Jin, Y., Kinetics of coupled primary- and secondary-minimum deposition of colloids under unfavorable chemical conditions, Environ. Sci. Technol. 41, 6976-6982 (2007).

Shen, C., Huan, Y., Li, B., Jin Y., Predicting attachment efficiency of colloid deposition under unfavorable attachment conditions, Water Resour. Res. 46, W11526, doi:10.1029/2010WR009218, (2010)

Stewart, P.S., Diffusion in biofilms, Journal of Bacteriology 185(5), 485–1491 (2003)

Sokolov, I.M., Klafter, J., Continuous-time random walks in an oscillating field: Field-induced dispersion and the death of linear response, Chaos, Solitons and Fractals 34, 81–86 (2007)

Tiukinhoy-Laing, S.D., Huang, S., Klegerman, M., Holland, C.K., McPherson, D.D., Ultrasound-facilitated thrombolysis using tissue-plasminogen activator-loaded echogenic liposomes. Thrombosis Research 119(7), 777-784 (2006).

Thomas, J.M. and Chrysikopoulos, Experimental investigation of acoustically enhanced colloid transport in water-saturated packed columns. Journal of Colloid and Interface Science 308, 200-207 (2007).

Tong, M., Johnson, W.P., Colloid population heterogeneity drives hyperexponential deviation from classic filtration theory, Environ. Sci. Technol. 41, 493-499 (2007).

Vogler, T., and Chrysikopoulos, C.V., Experimental investigation of acoustically enhanced solute transport in porous media. Geophysical Research Letters 29(15), 1710 (2001).

Wang, Y., Huo, M., Li, Q., Fan, W., Yang, J., Cui, X., Comparison of clogging induced by organic and inorganic suspended particles in a porous medium: implications for choosing physical clogging indicators, Journal of Soils and Sediments 5, (2018)

Wang, Z., Taylor, S.E., Sharma, P., Flury, M., Poor extraction efficiencies of polystyrene nano- and microplastics from biosolids and soil, PLoS ONE 13(11), e0208009 (2018).

You, Z., Badalyan, A., Bedrikovetsky, P., Size-Exclusion colloidal transport in porous media-stochastic modeling and experimental study., SPE Journal, 162941 (2013).

Zhang, Z., Nadezhina, E., Wilkinson, K.J., Quantifying diffusion in a biofilm of streptococcus mutans, Antimicrobial Agents And Chemotherapy 55(3), 1075–1081 (2011)